Chiral spintronics: non collinear spin textures with application to Racetrack Memory

Stuart Parkin

Max-Planck Institute for Microstructure Physics
Halle (Saale)

Martin Luther University
Halle-Wittenberg

stuart.parkin@mpi-halle.mpg.de


Andriy Styervoyedov
Kyryolo Dronov
Tianping Ma
Rana Saha
Yuecheng Zhuang
Tianping Ma, Rana Saha, Abhay Srivastava, Ajaya Nayak,
Robin Blasing, Peter Werner
Max Pianck Institute MSP, Halle
Vivek Kumar, Roshnee Sahoo, Parul Devi, Claudia Felser
Max Planck Institute cpfs, Dresden
Börge Göbel, Ingrid Mertig
Martin Luther University, Halle
See-Hun Yang, Chirag Garg
IBM Research – Almaden, San Jose, California

Spintronics – from materials and phenomena to applications

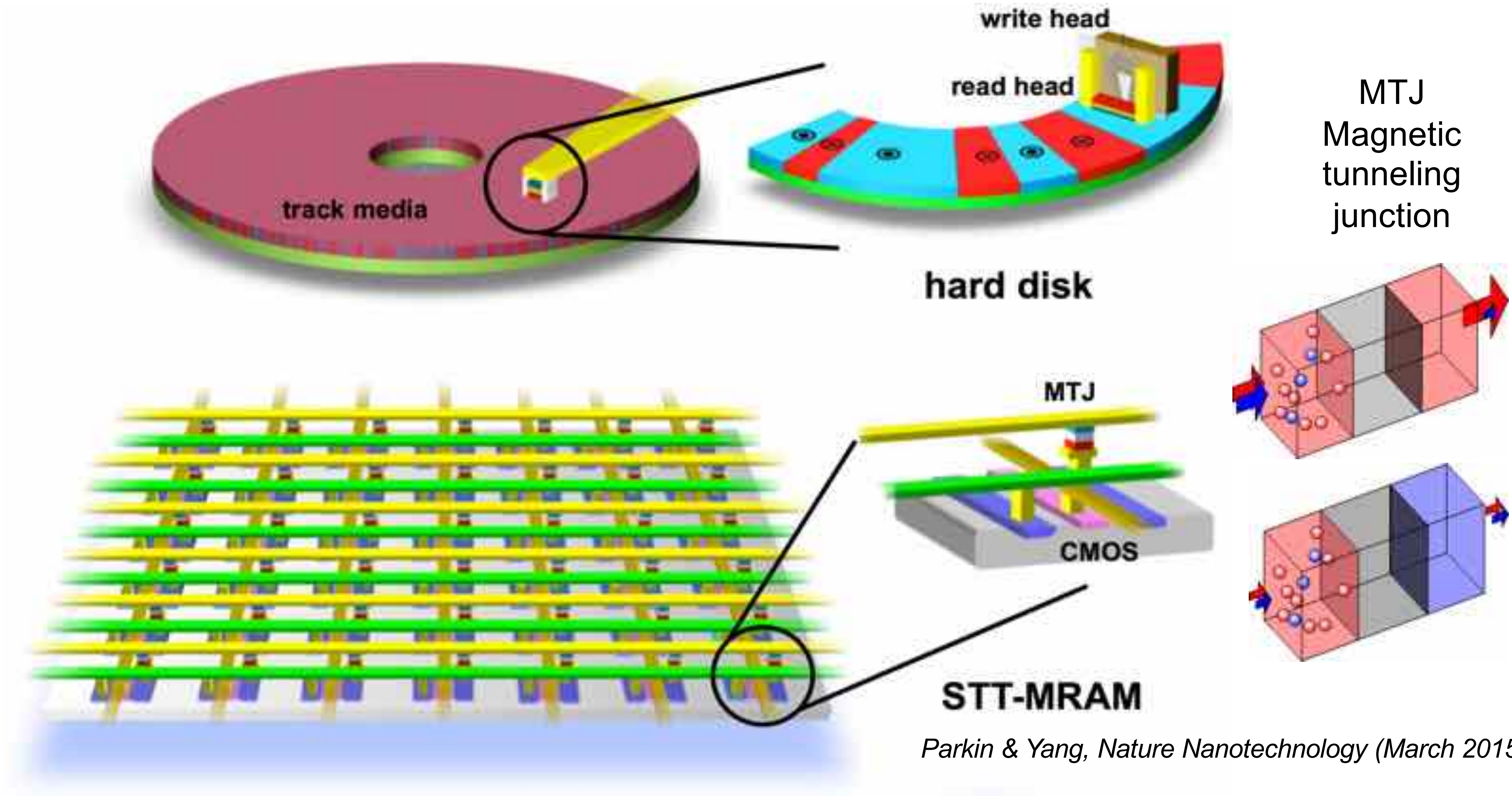

Parkin & Yang, Nature Nanotechnology (March 2015)

Spintronic technologies evolution

HDD Spin Valve & MTJ read heads

1988-1991

GMR
Spin Engineering
- Oscillatory interlayer coupling
- Co/Cu
- Interface spin-dependent coupling
- Dusting layers

1997

Spin-valve recording heads (mass-production)

2007

Magnetic Tunnel Junction recording heads (mass production)

2015

Slow-down of increased HDD capacity

MRAM

1995

MTJ based MRAM proposal

1996

Spin transfer torque (STT switching

1999

1 kbit array
High MR
Low RA
0.25 μm
2.3 ns R/W

2001

Giant TMR using MgO

2005

16 Mbit demonstrator (180nm CMOS)
Field switched

2019

Samsung announces shipment of high-performance foundry 28nm CMOS STT e-MRAM

Magnetic Racetrack Memory

- Bits = Domains in the tracks

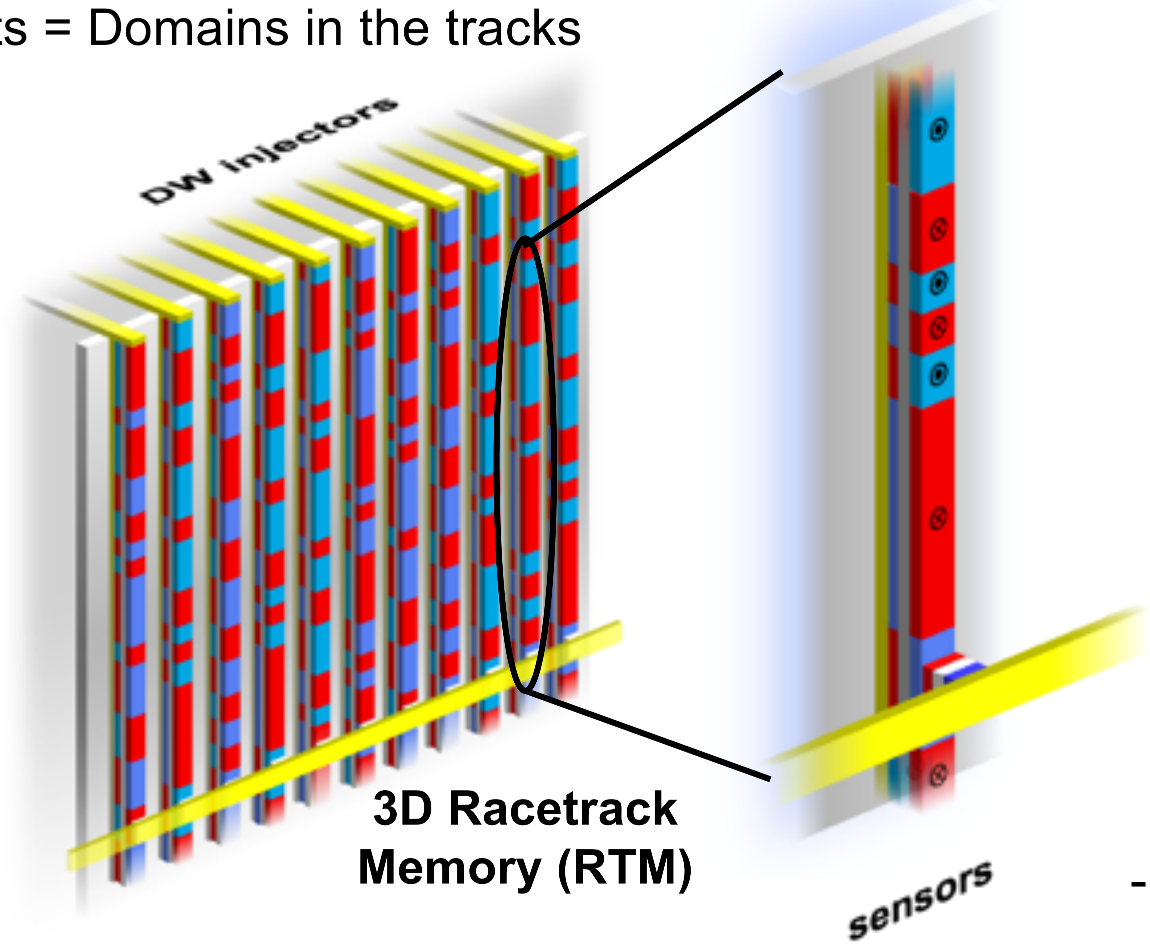

Parkin, US patents 6834005, 6898132 (2004)
*Parkin et al., Science **320**, 190 (2008)*
Parkin, Scientific American (2009)

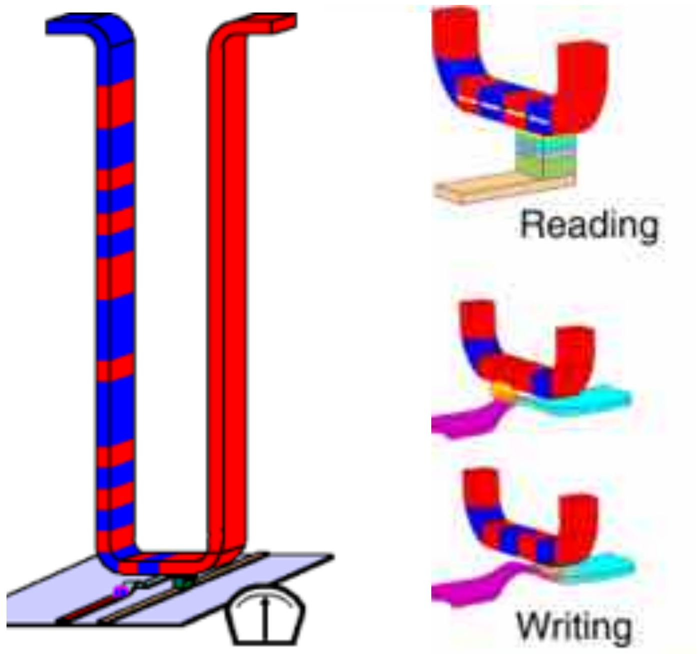

- A novel *three-dimensional* storage-class memory

- The capacity of a hard disk drive

Memory on Racetrack!
4+ stages

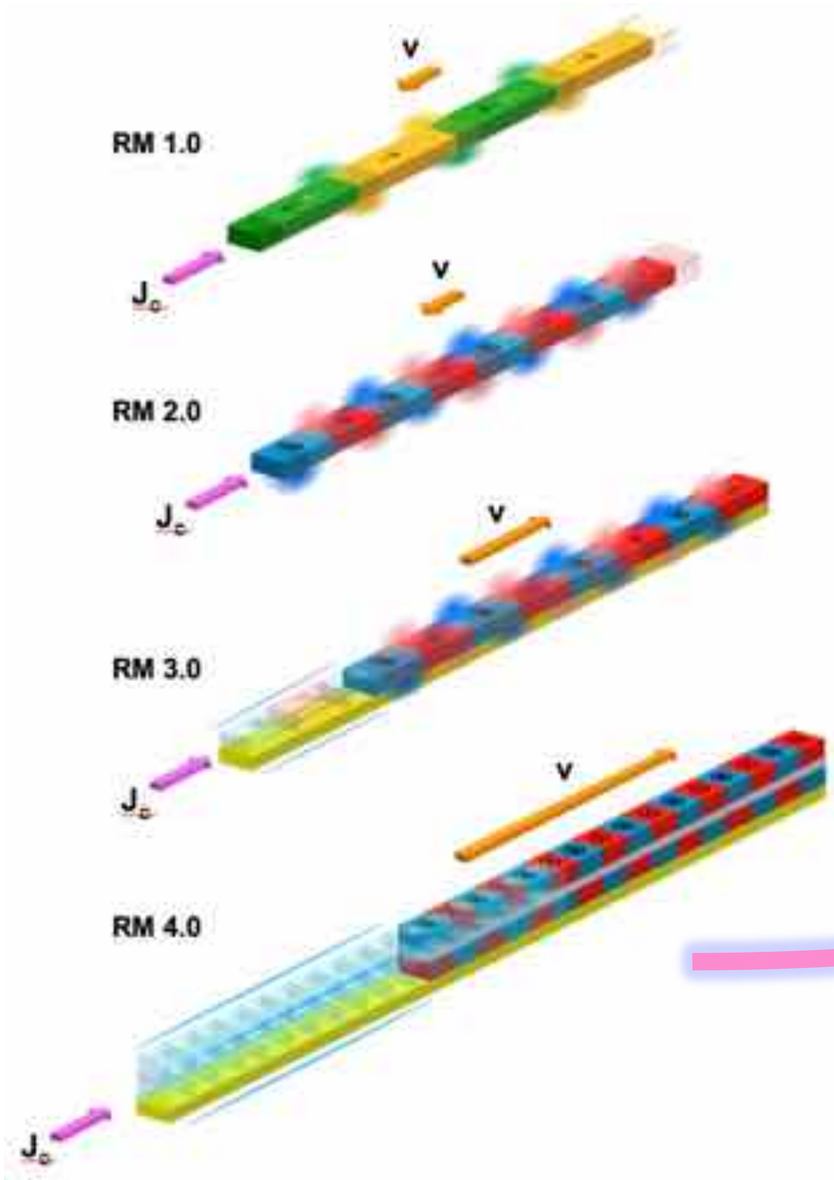

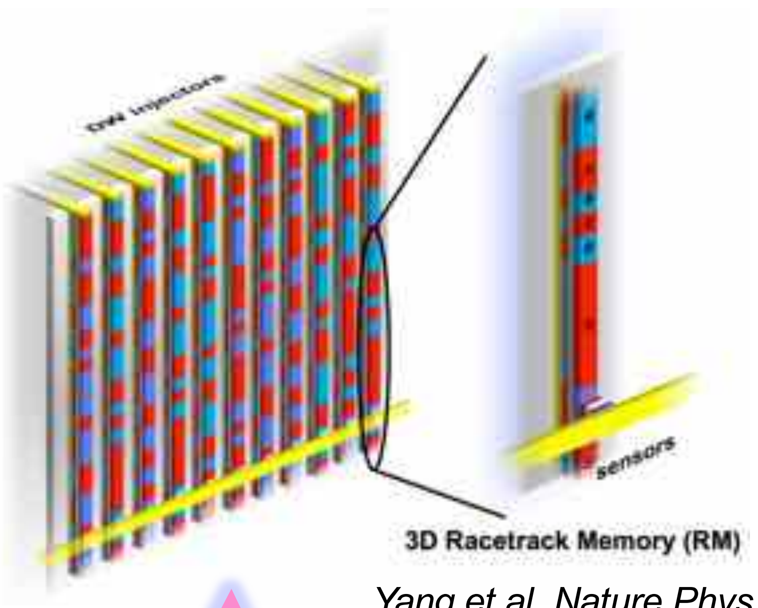

Yang et al. Nature Phys. (2019)
Bläsing et al. Nature Commun. (2018)
Garg et al. Nature Commun. (2018)
Filippou et al. Nature Commun. (2018)
Garg et al. Science Adv. (2017)
Parkin & Yang, Nature Nano. (2015)
Yang, Ryu and Parkin, Nature Nano. (2015)
Ryu et al. Nature Nano. (2013)
Parkin et al. Science (2008)

Chiral domain walls from Dzyaloshinskii-Moriya Interaction

(#1) Perpendicular Magnetic anisotropy (PMA)

- materials: Co/Ni, Co/Pt, Co/Pd, RE/TM multilayers, low symmetry magnetic materials
- racetracks magnetized perpendicular to the plane of the racetrack

- *Bloch* and *Neel* domain walls
  → *narrow* domain walls

- Dzyaloshinskii-Moriya Interaction
  → *chiral* domain walls

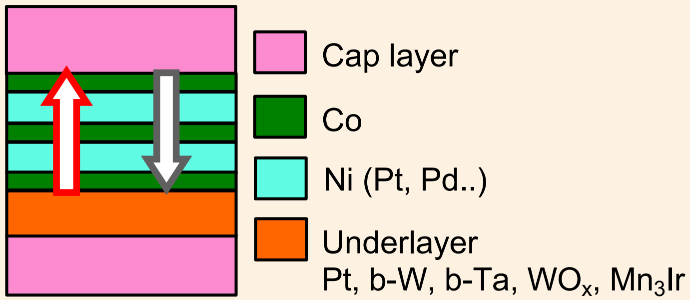

Neel domain walls

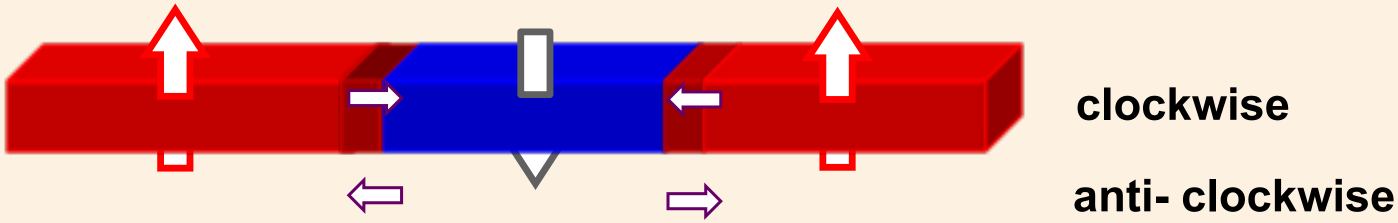

(#2) Dzyaloshinskii–Moriya interaction (DMI)

- *chirality* of domain walls set by interface(s) vector exchange interaction

(#3) Proximity Induced Magnetization (PIM)

(#4) Spin Hall effect: conversion of charge to spin current

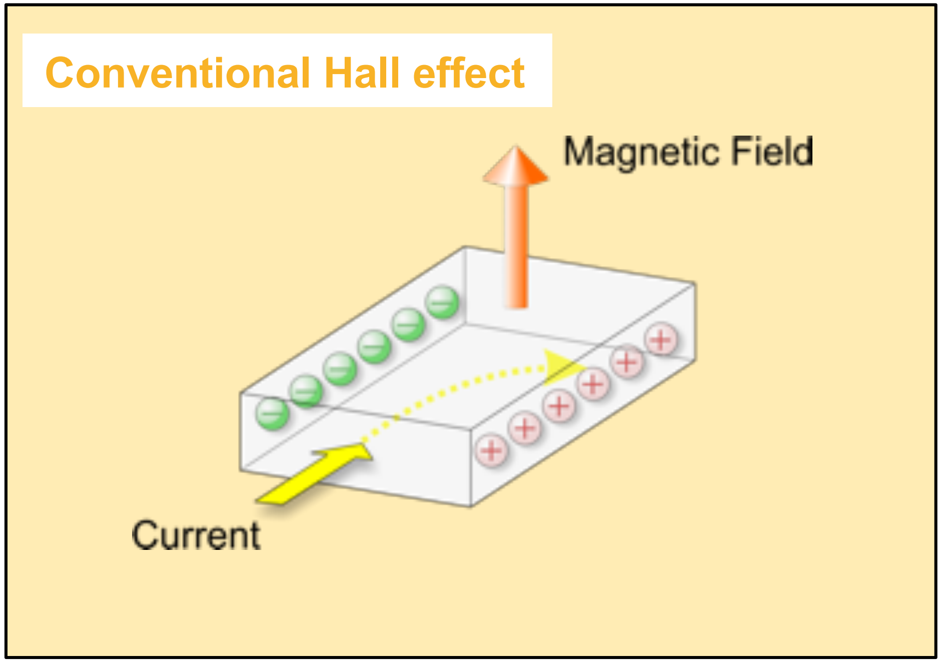

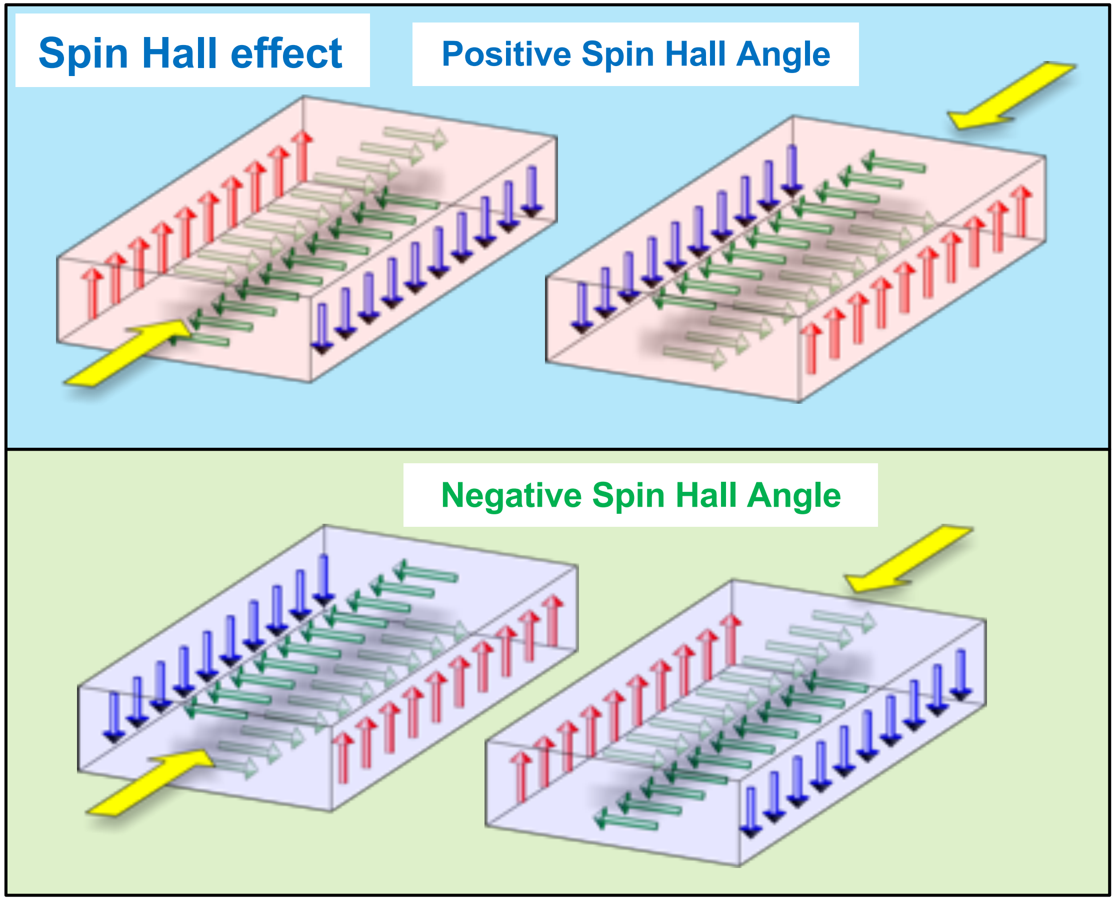

SHA: Spin Hall Angle
charge to spin conversion efficiency: ~10-30 %

Charge to spin conversion via the Spin Hall Effect

- Spin Hall effect: dramatic evolution over past 5 years
- Novel materials show large spin Hall effect
  - Triangular antiferromagnets
  - Novel crystalline phases
- Important technological applications
  - Racetrack – DW velocities > 1,000 m/sec
  - 3T Single DW Racetrack - replacement for SRAM

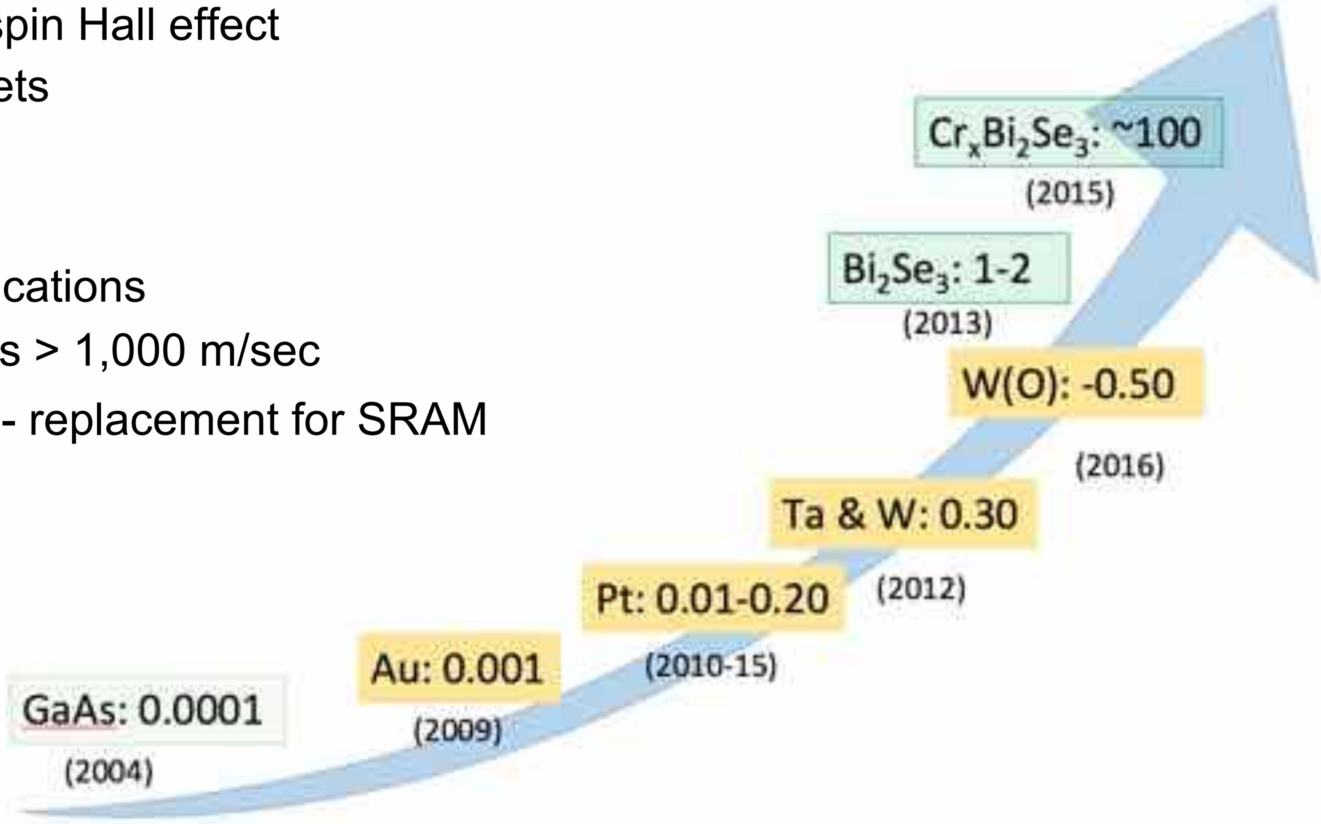

Zhang *et al.* Nat. Phys. (2015)
Demasius *et al.*, Nat. Comm. (2016)
Nayak *et al.* Sci. Adv. (2016)
Zhang *et a.* Sci. Adv. (2016)

RM 4.0: Very High DW Speeds in Synthetic Antiferromagnet (SAF) racetracks

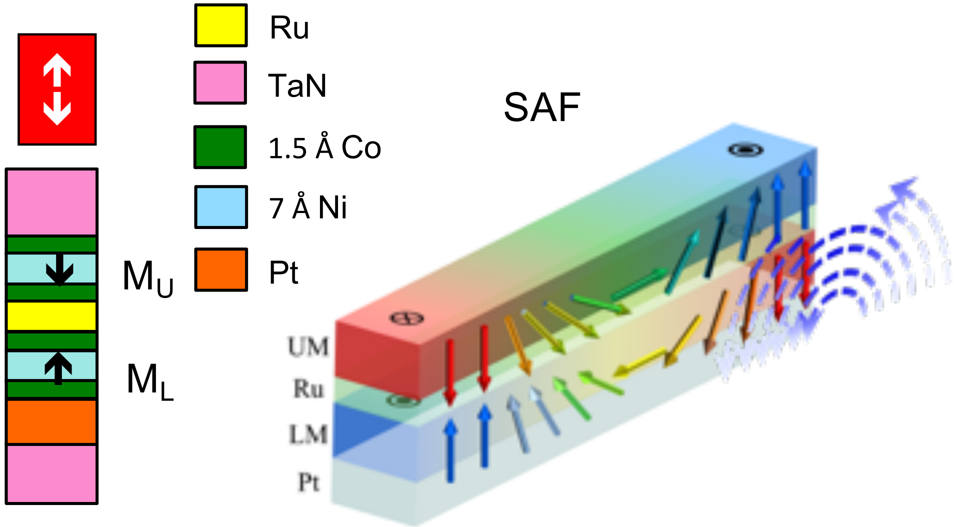

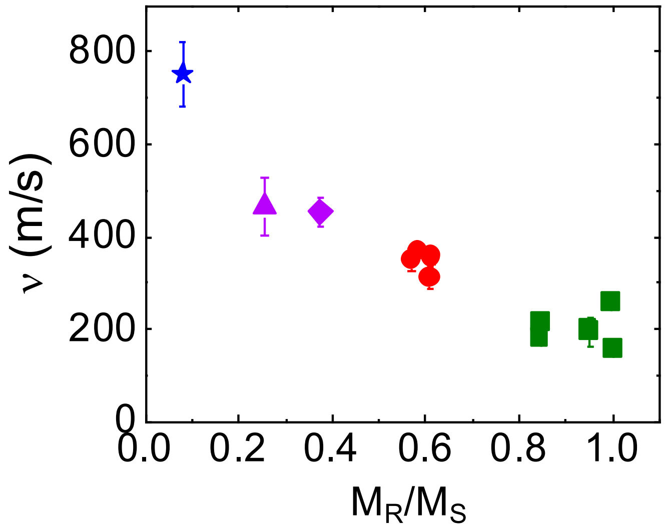

→ SAF: Synthetic antiferromagnet: upper racetrack = exact mirror image of lower
→ DW velocity increases as degree of compensation of moments in upper and lower racetracks increased
→ 4x highest DW velocity yet reported → Speeds exceed 1.5- 5 km/sec
→ AF exchange field > DMI field

Yang et al. Nature Nanotechnology (2015)

Racetrack Memory 4.0

→ 20 domain walls moved in lock step with current pulses
→ High velocity at low current densities
→ Narrow domain walls (~6 nm)
→ Very thin racetracks (~1 nm)

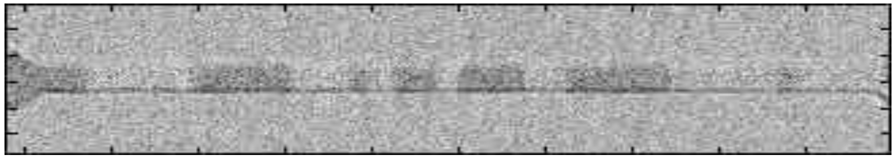

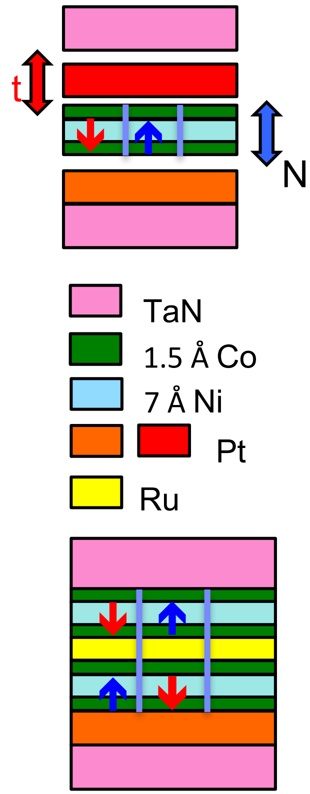

→ Giant domain wall velocities in Synthetic Antiferromagnet racetracks > 1 km/sec

Domain wall motion: complex interplay of 4 spin-orbit derived phenomena

1. Perpendicular magnetic anisotropy
2. Proximity induced magnetization
3. Chiral domain walls – DMI
4. Spin currents – from spin Hall effect (SHE)

Ryu et al. Nature Nanotechnology (2013)
Yang et al. Nature Nanotechnology (2015)
Parkin et al. Nature Nanotechnology (2015)
Garg et al. Sci. Adv. (2017); Nat. Comm. (2018)
Yang et al. Nat. Phys. (2019)

Heusler Family of compounds

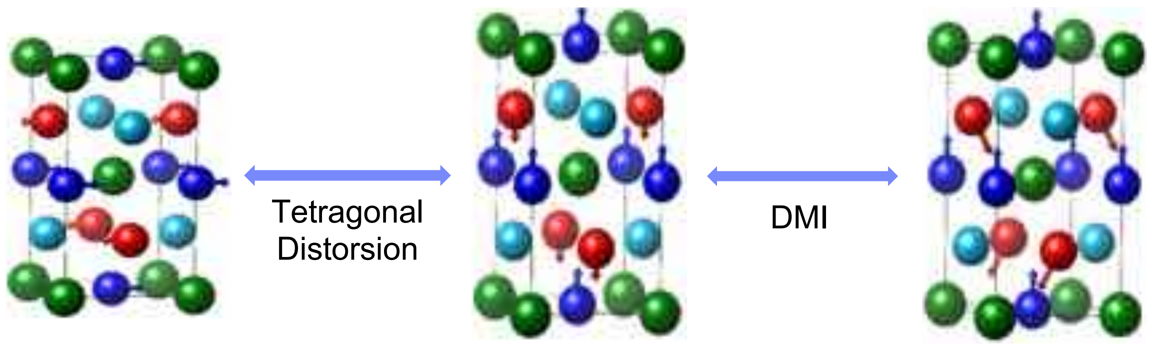

In-plane Magnetization

Out-of-plane Magnetization

Non-collinear Magnet

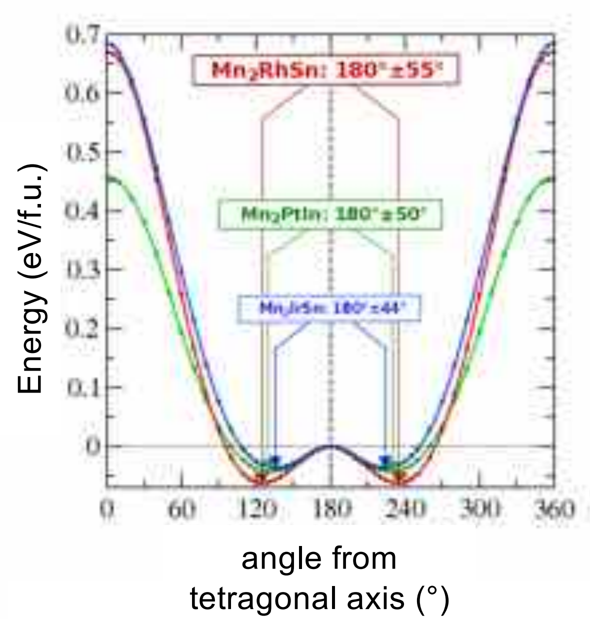

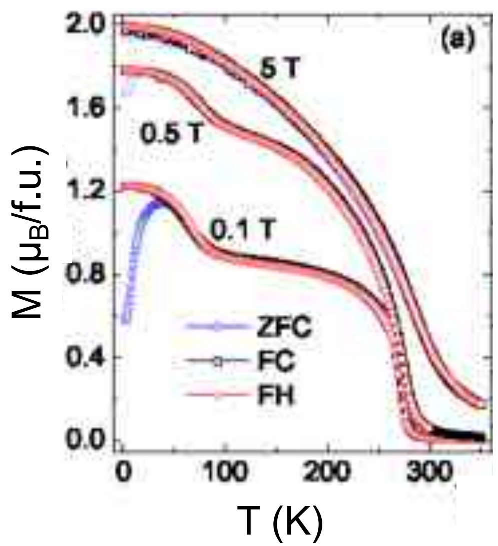

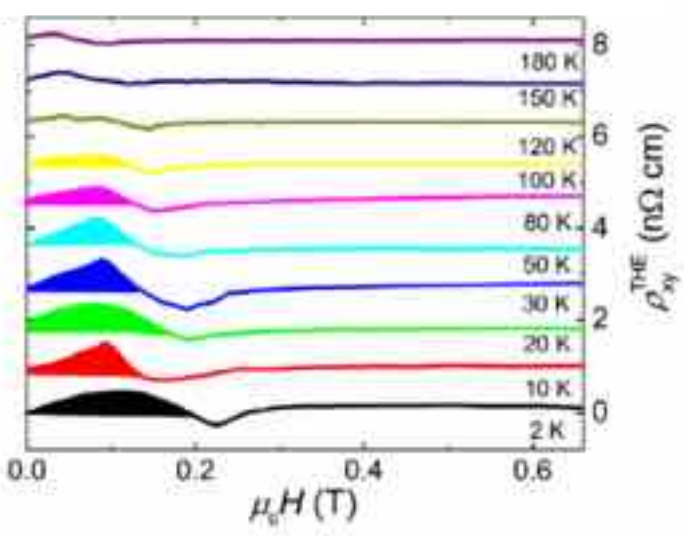

Mn_2RhSn

Also Mn_2IrSn, **Mn_2PtSn**

Claudia Felser et al.

Meshcheriakova, *et al.*
Phys. Rev. Lett. **113,** 087203 (2014)

Rana *et al.* New J. Phys. **18**, 85007 (2016)

Skyrmions and anti-skyrmions

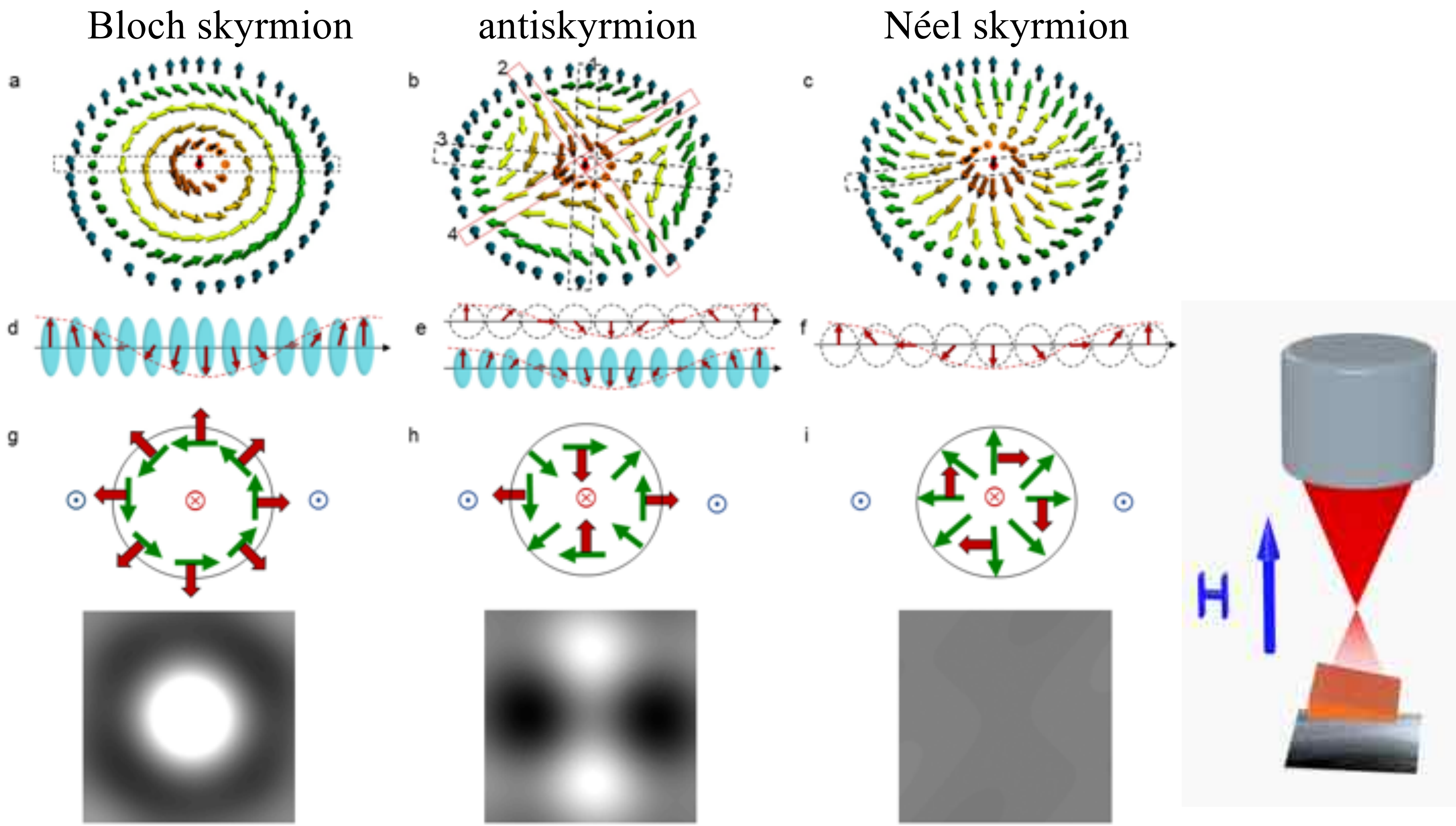

Mn$_{1.4}$Pt(Pd)Sn

Anti-Skyrmions

- stable above 300 K

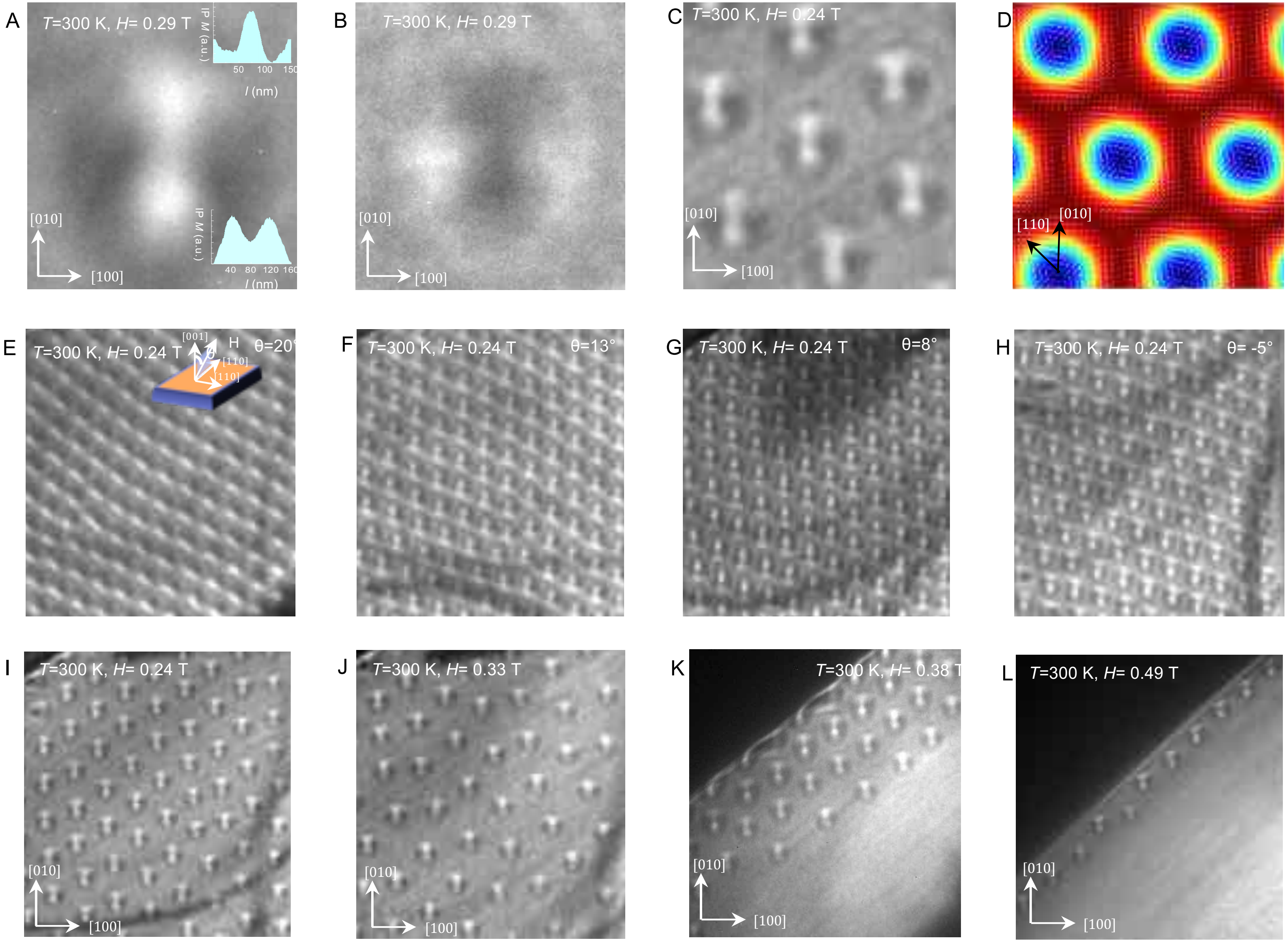

Nayak *et al.*
Nature (2017)

Stabilization of anti-skyrmion lattice in wedge-shaped lamella of $Mn_{1.4}Pt_{0.9}Pd_{0.1}Sn$

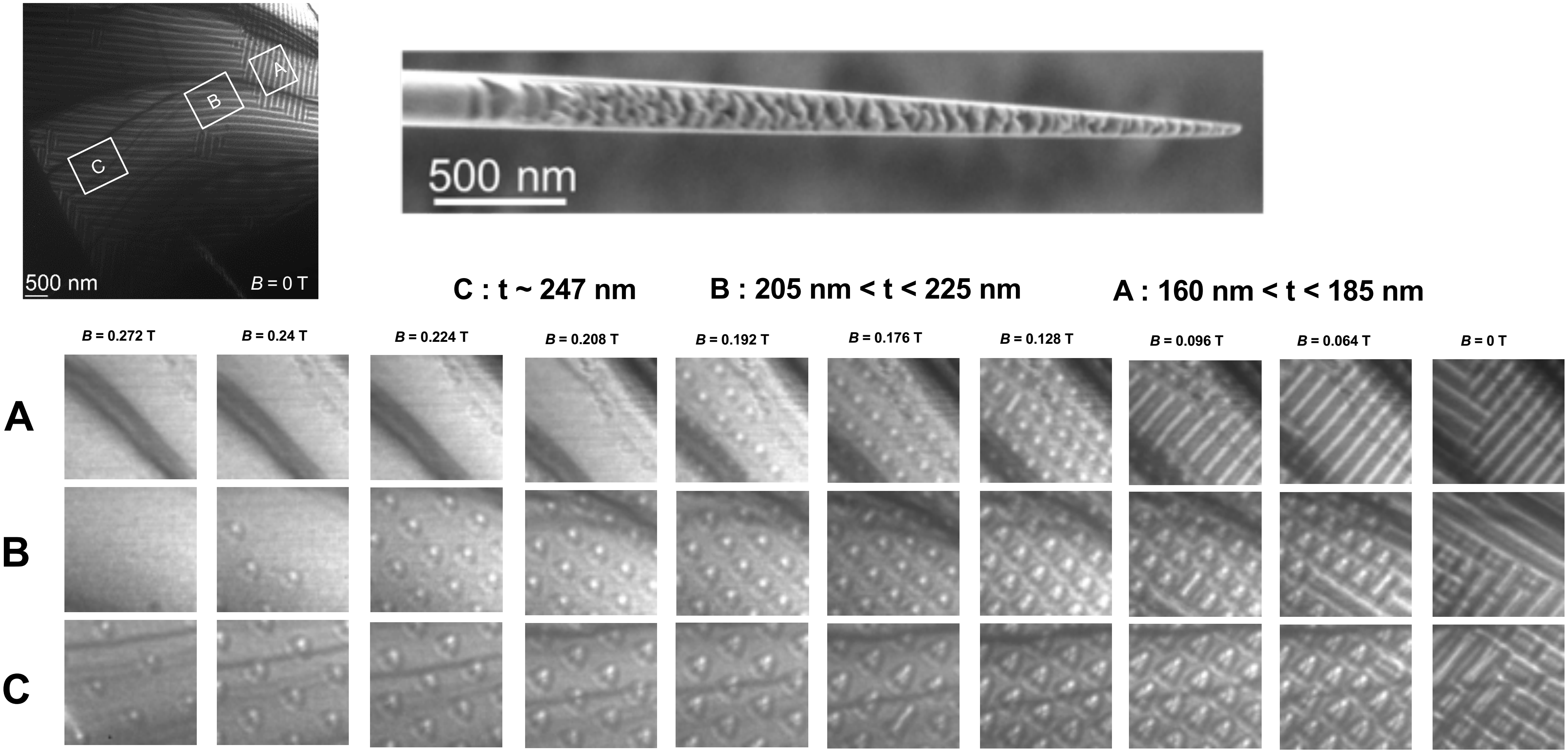

$Mn_{1.4}(Pt_{0.9}Pd_{0.1})\,Sn$

A : 160 nm < t < 185 nm

B : 205 nm < t < 225 nm

C : t ~ 247 nm

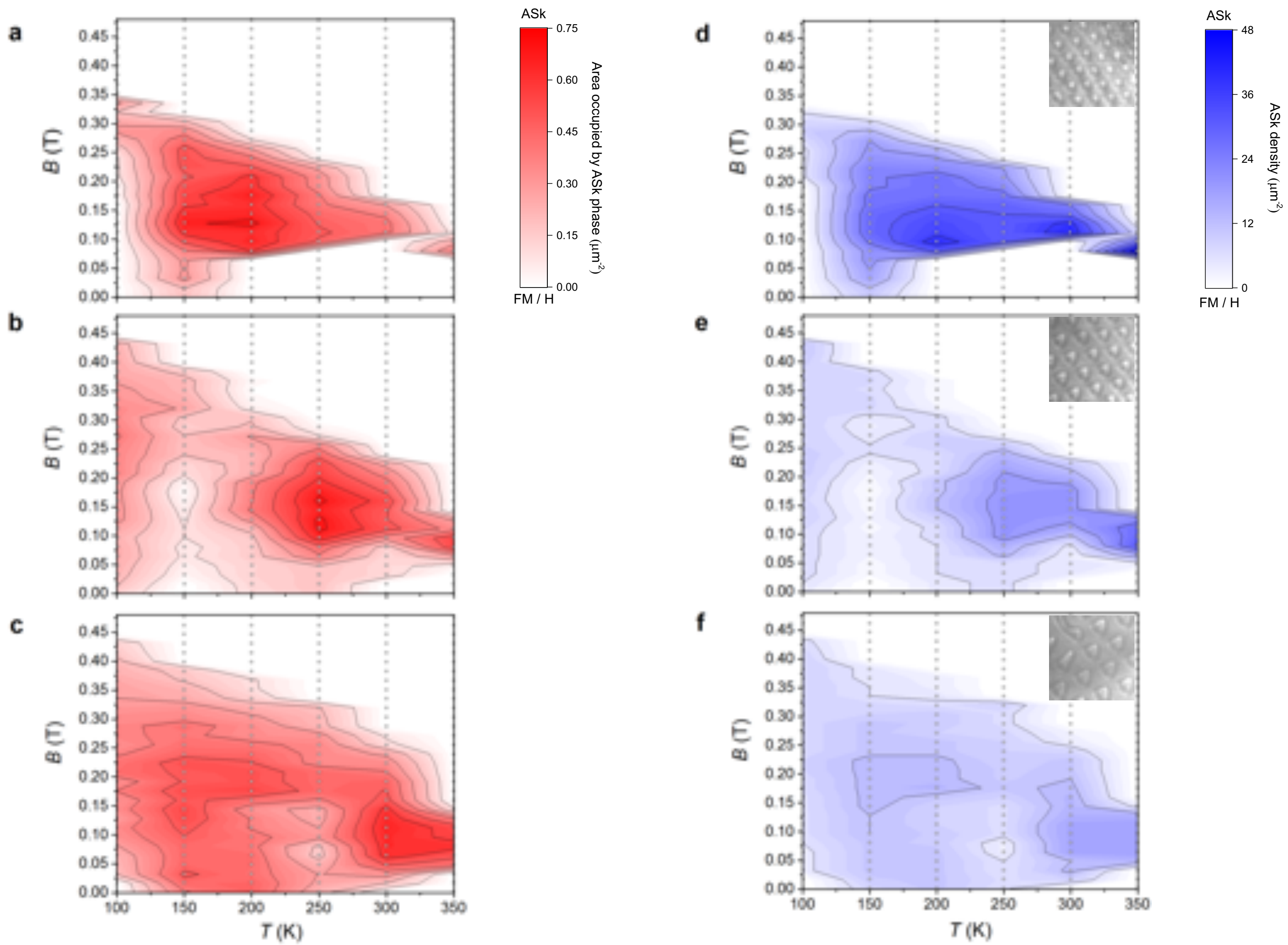

Magnetic phase diagram of wedge-shaped lamella of single crystalline $Mn_{1.4}Pt_{0.9}Pd_{0.1}Sn$ after field-cooling (FC) process with 0.2 T applied at 365 K.

Magnetic phase diagram of skyrmions: FeGe (B20, chiral)

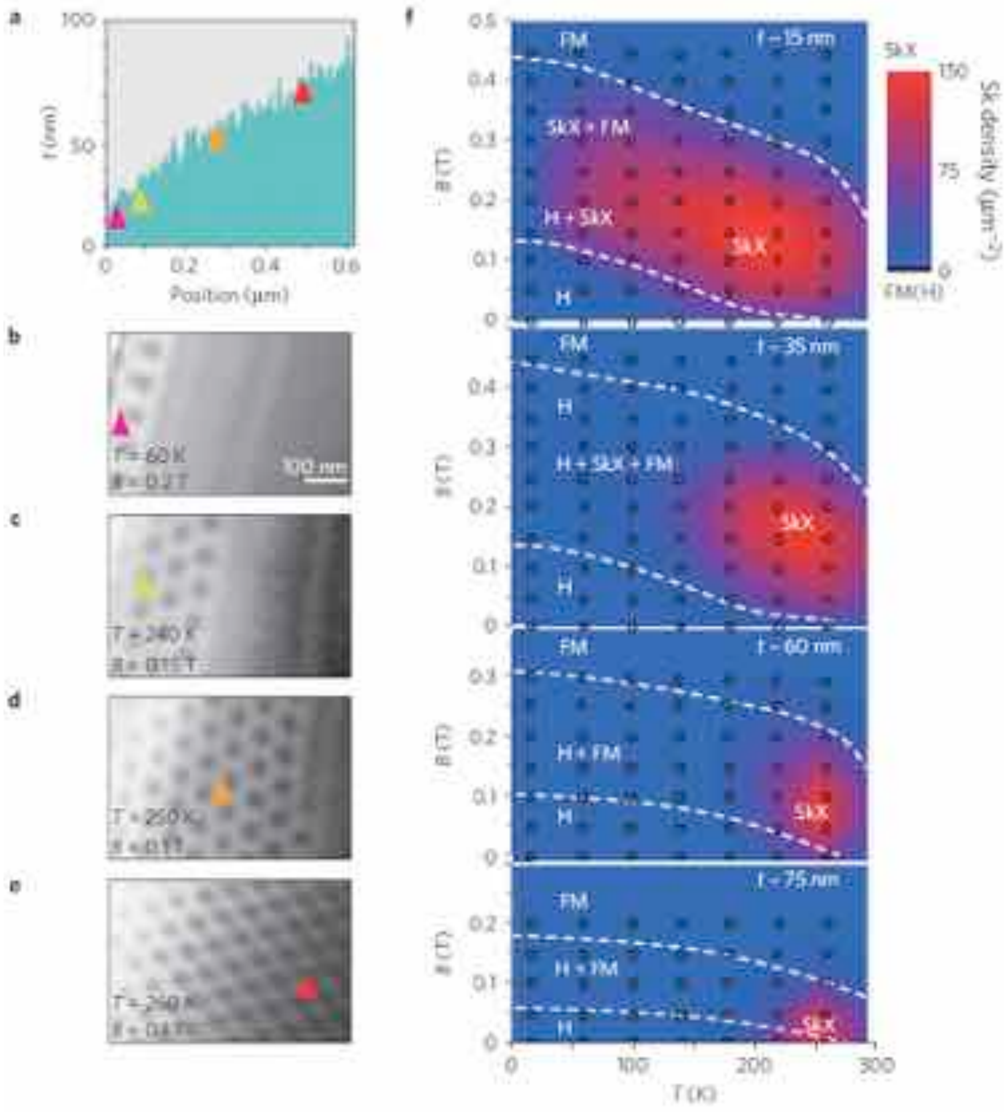

→ Anti-skyrmions are stable over wide range of temperature and magnetic fields as compared to skyrmions

→ Skyrmions are more stable at lower thicknesses

X. Z. Yu , Y. Tokura *et al.*, Nat. Mater. 10, 106, (2011)

Thickness and field dependent phase diagram of B20 and D2d structures

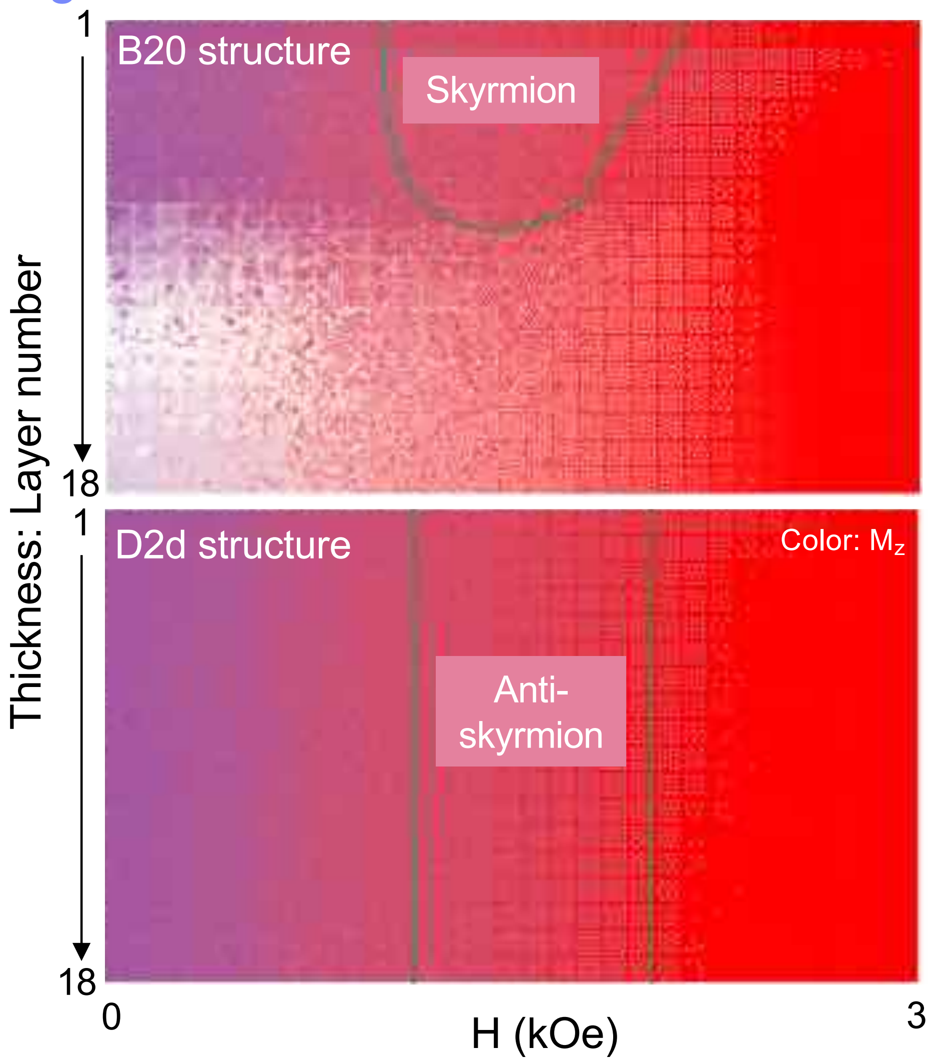

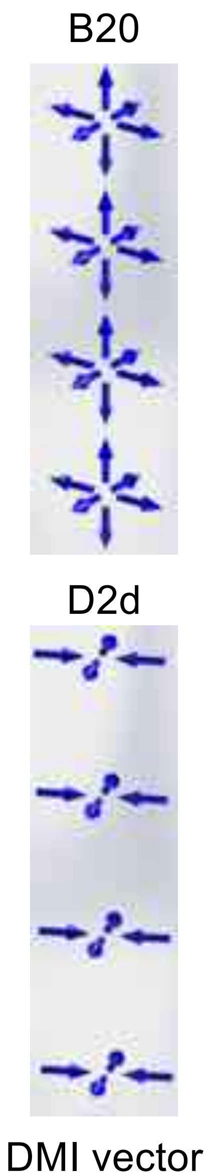

$$H_{B20} = -J\sum_r \vec{S}_r \cdot \left(\vec{S}_{r+a\hat{x}} + \vec{S}_{r+a\hat{y}} + \vec{S}_{r+a\hat{z}}\right) - \vec{H}\cdot\sum_r \vec{S}_r$$
$$-D_{B20}\sum_r\left(\vec{S}_r\times\vec{S}_{r+a\hat{x}}\cdot\hat{x} + \vec{S}_r\times\vec{S}_{r+a\hat{y}}\cdot\hat{y} + \vec{S}_r\times\vec{S}_{r+a\hat{z}}\cdot\hat{z}\right)$$

Magnetization modulated along thickness, due to z component of DMI.

→ Twisted Skyrmion tube preferred.

→Skyrmions not stable when thickness is too large (twist from surface to center larger than $\pi/2$).

$$H_{D2d} = -J\sum_r \vec{S}_r \cdot \left(\vec{S}_{r+a\hat{x}} + \vec{S}_{r+a\hat{y}} + \vec{S}_{r+a\hat{z}}\right) - \vec{H}\cdot\sum_r \vec{S}_r$$
$$-D_{D2d}\sum_r\left(-\vec{S}_r\times\vec{S}_{r+a\hat{x}}\cdot\hat{x} + \vec{S}_r\times\vec{S}_{r+a\hat{y}}\cdot\hat{y}\right)$$

Magnetization unchanged along thickness, due to Heisenberg exchange.

→ Untwisted Anti-Skymion tube preferred.

→ Anti-Skyrmion remain stable to large thicknesses.

Thickness dependence of helical periodicity in wedge-shaped lamella ($Mn_{1.4}Pt_{0.9}Pd_{0.1}Sn$)

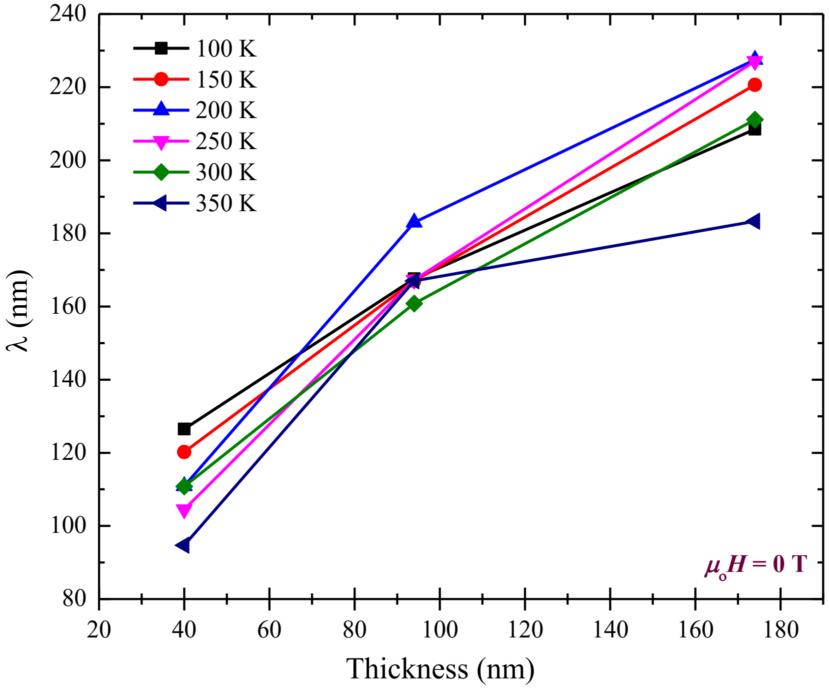

Helical periodicity increases with thickness

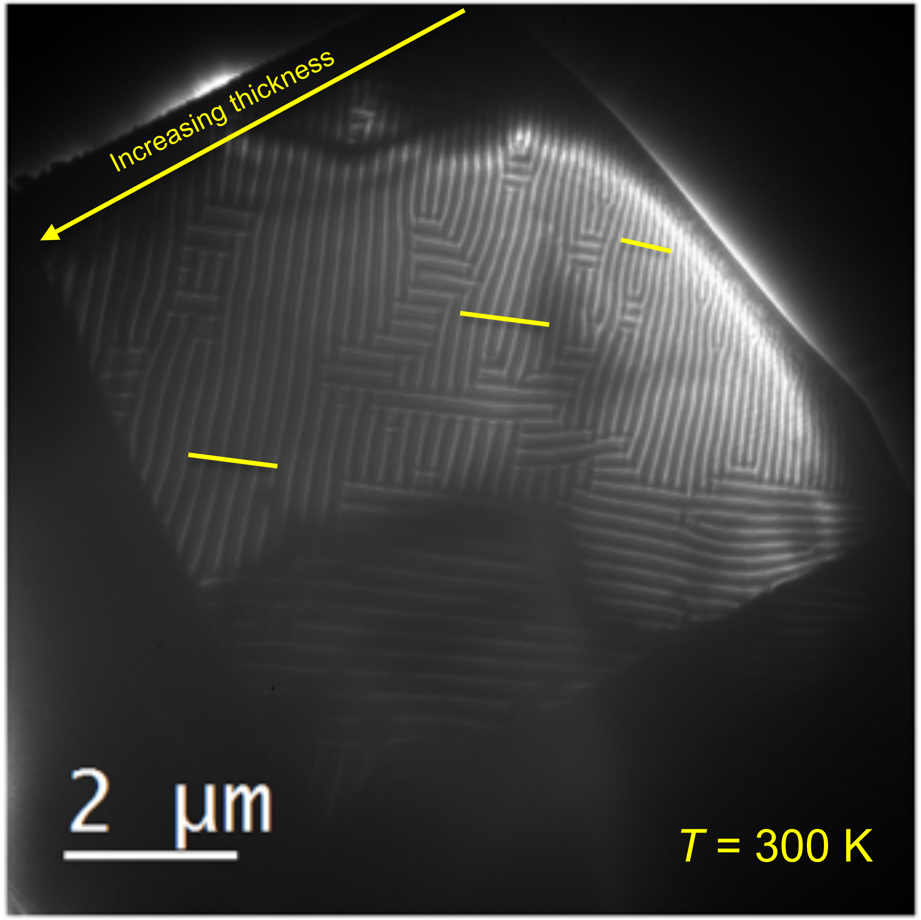

Variable temperature magnetic force microscopy imaging of helical phase

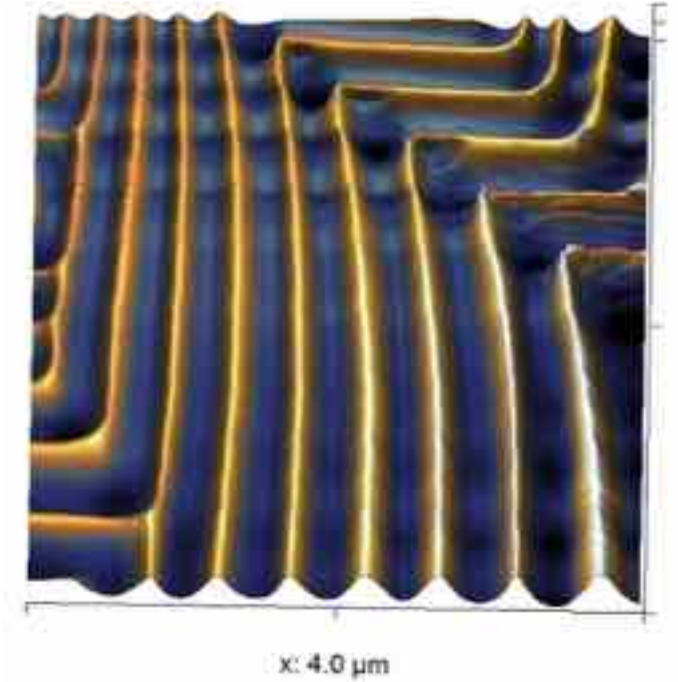

line profile

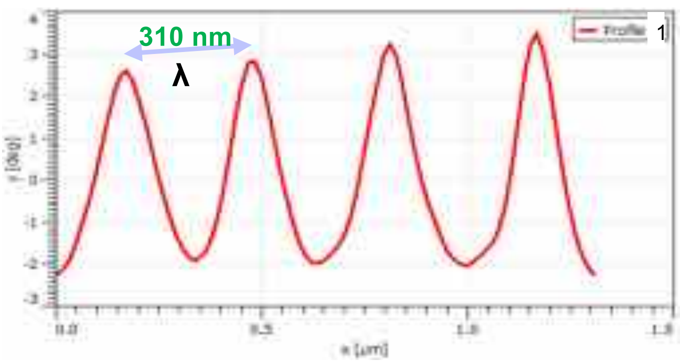

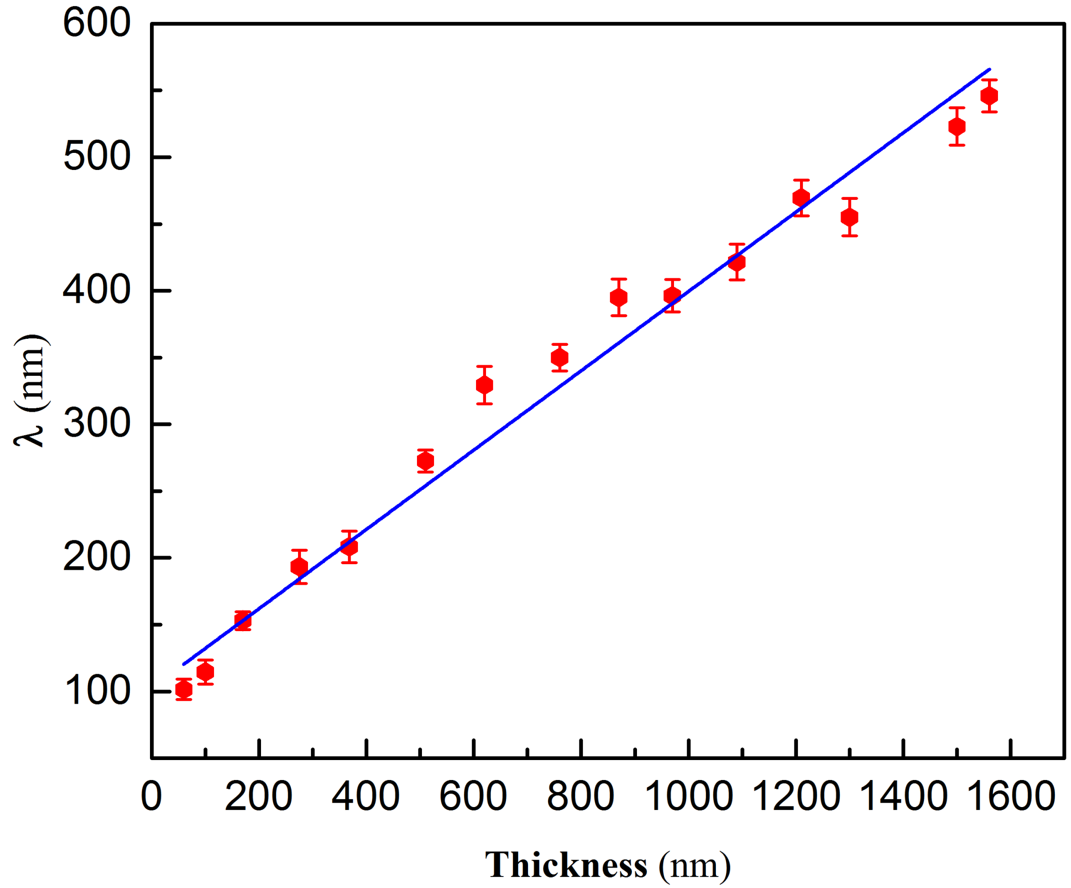

→ Helical wavelength λ increases linearly with thickness from 80 nm to 1600 nm

Variable temperature MFM: helical wavelength vs thickness up to 4 microns

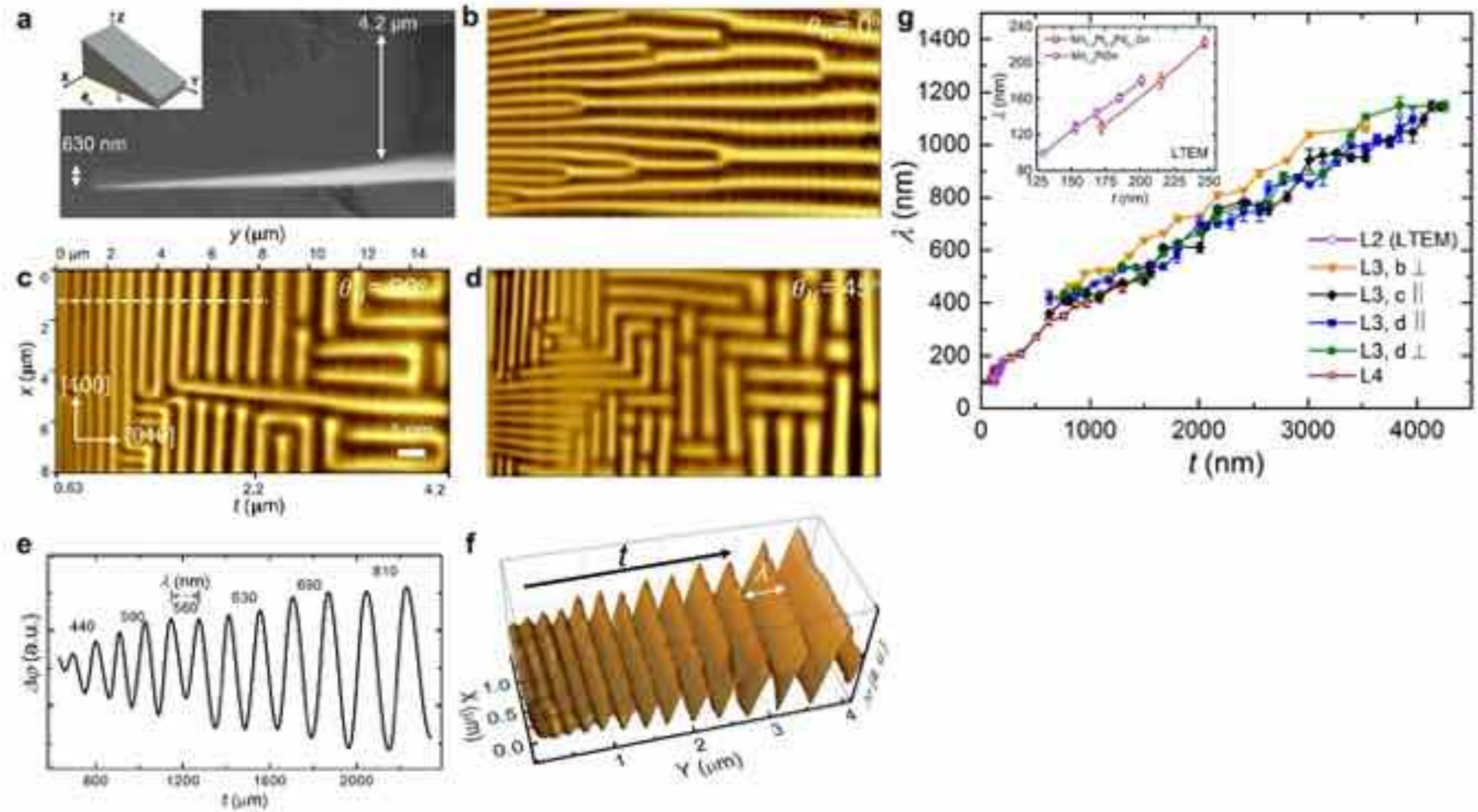

Magnetic force microscopy (MFM) image of helical magnetic phase in a wedge-shaped lamella of single crystalline $Mn_{1.4}PtSn$ at 300 K in zero magnetic fields and Helical wavelength vs. thickness of the lamella crystal.

Variable temperature MFM: aSk size vs thickness up to 4 microns

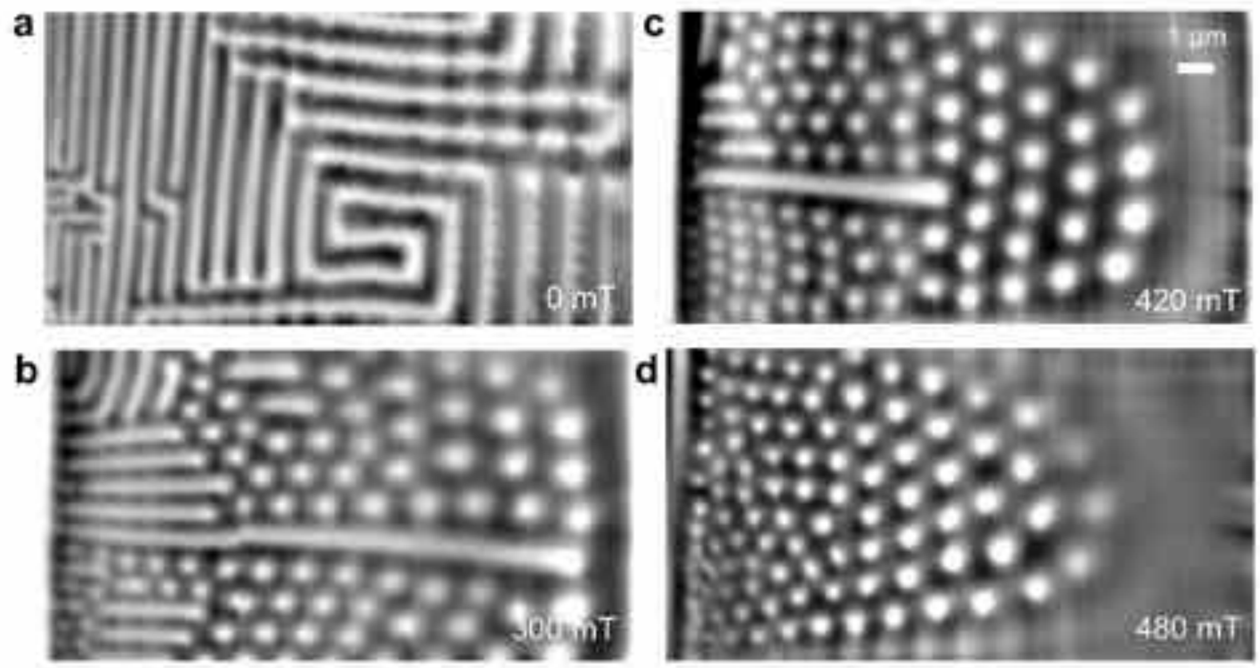

Magnetic force microscopy (MFM) image of magnetic field dependence of Antiskyrmion

- Thickness of the lamella increases from left end to right. The size of the images are 8×16 μm.

- Maximum size of the antiskyrmion is found to be 1.16 μm.

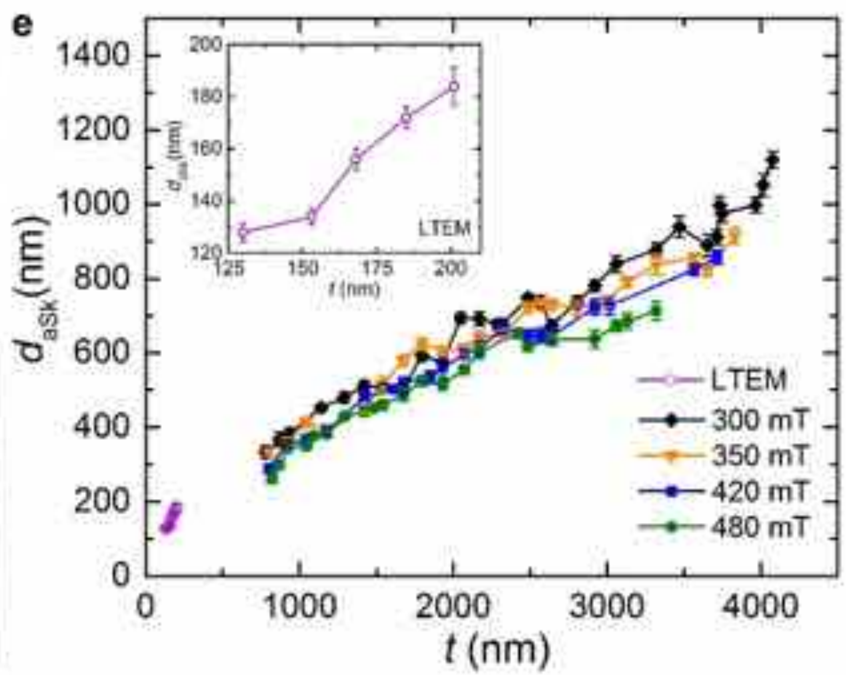

Antiskyrmion size vs. thickness 300 K

Anti-skyrmion → elliptical skyrmion due to dipole-dipole interaction

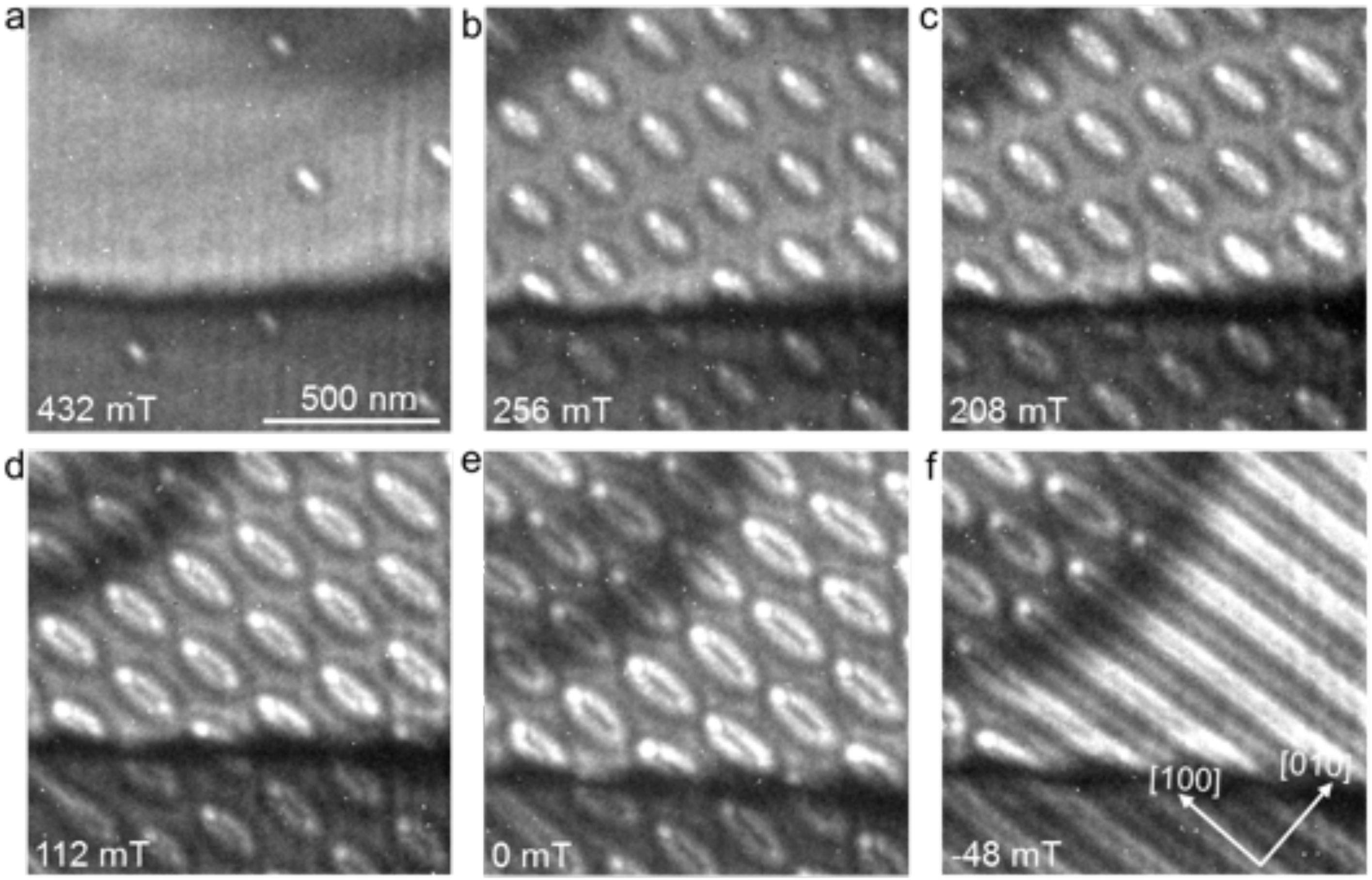

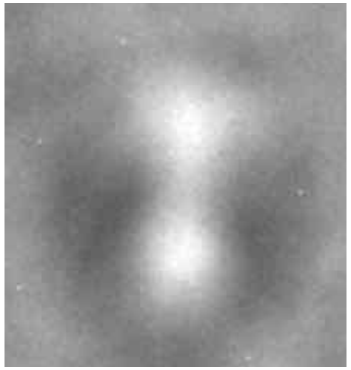

→ Metastable elliptical Bloch skyrmions can be stabilized in same material

PtMnGa: crystal structure (buckled layered)

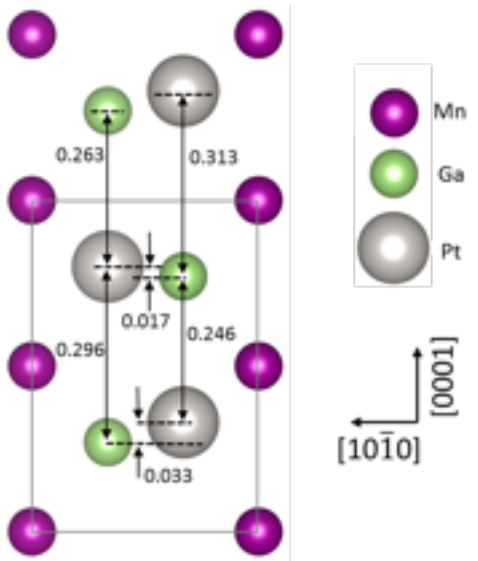

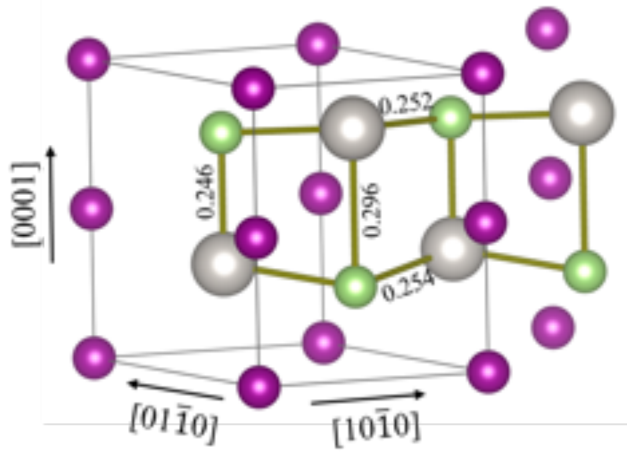

Crystal structure:

trigonal (P3m1, space group no. 156)

Lattice Parameters:

a=b= 4.35Å, c= 5.59Å

α=β =90º, Ƴ= 120º

→ Isostructural to hourglass Fermion material KHgSb

H K L	$\|F_{obs}(HKL)\|^2$	$\|F_{calc}(HKL)\|^2$
0 0 1	**196.59**	**180.80**
0 1 1	6840.50	5999.50
0 2 1	2750.74	2577.01
-1 1 0	2646.92	2518.25
-1 1 1	3647.66	4349.99
-1 1 2	16313.61	11653.70
-1 2 0	29582.05	28119.56
-1 2 1	**124.15**	**85.47**
0 0 3	**518.51**	**654.83**
-1 3 0	**649.65**	**614.80**
-2 2 1	2081.43	3479.31
-2 2 2	3779.58	2752.53
0 2 2	4448.76	5720.66
-1 2 2	6201.97	8002.20
-2 2 0	1419.61	1180.43
-2 3 1	2616.53	1623.58
-1 2 4	2441.26	2914.10

Bold letters indicate observed reflections, which are forbidden in space group $P6_3/mmc$

PtMnGa: Lorentz TEM observation of Néel skyrmions

FC with 0.096 T
T = 100 K
H = 2.8 kOe
Δf = -1.5 mm

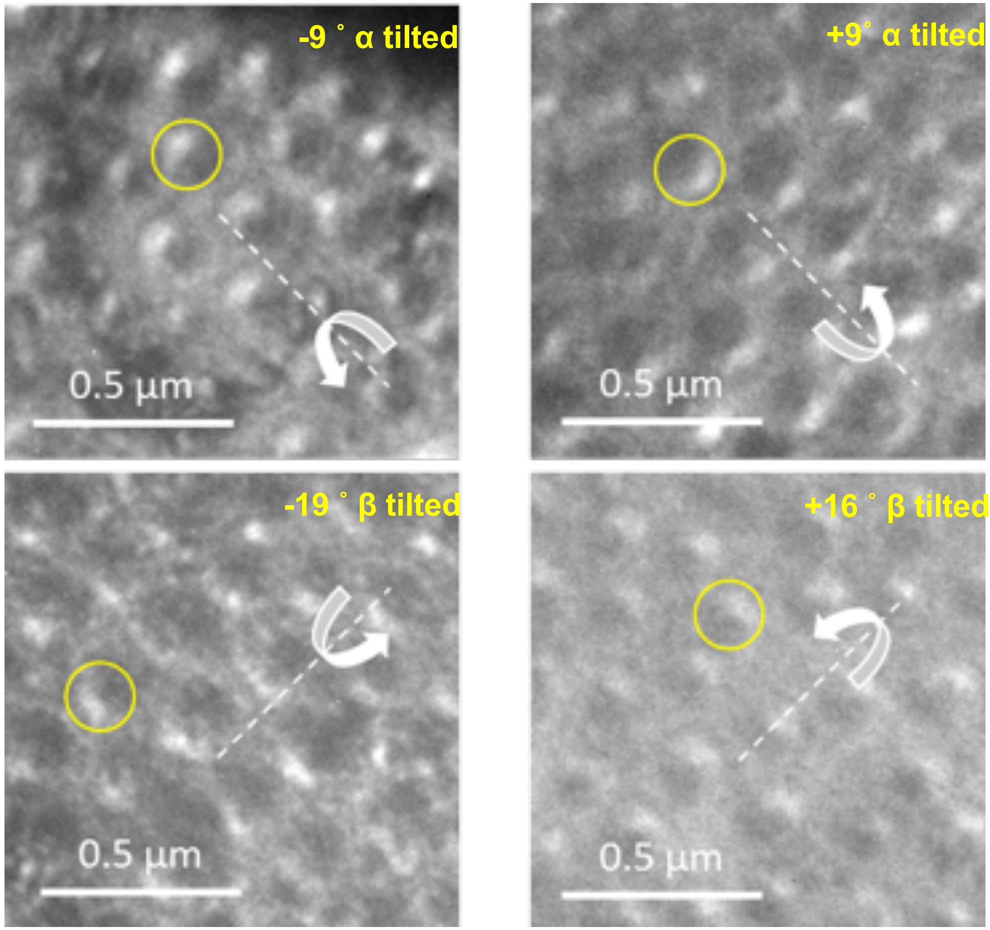

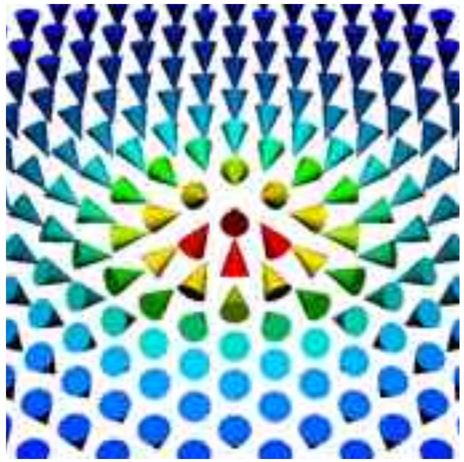

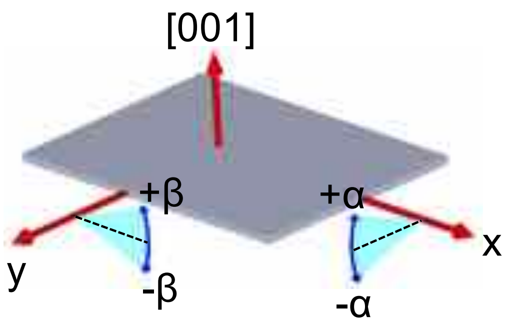

Stable Skyrmions for thicker layers observed using MFM

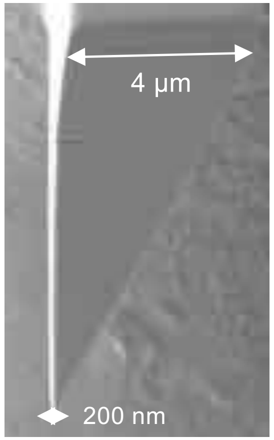

SEM side view image of the wedge-shaped lamella

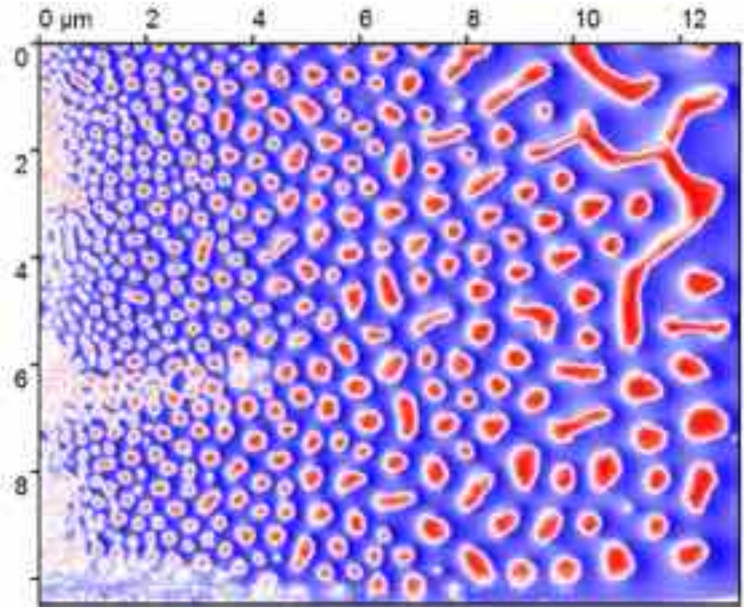

MFM image of Néel skyrmions

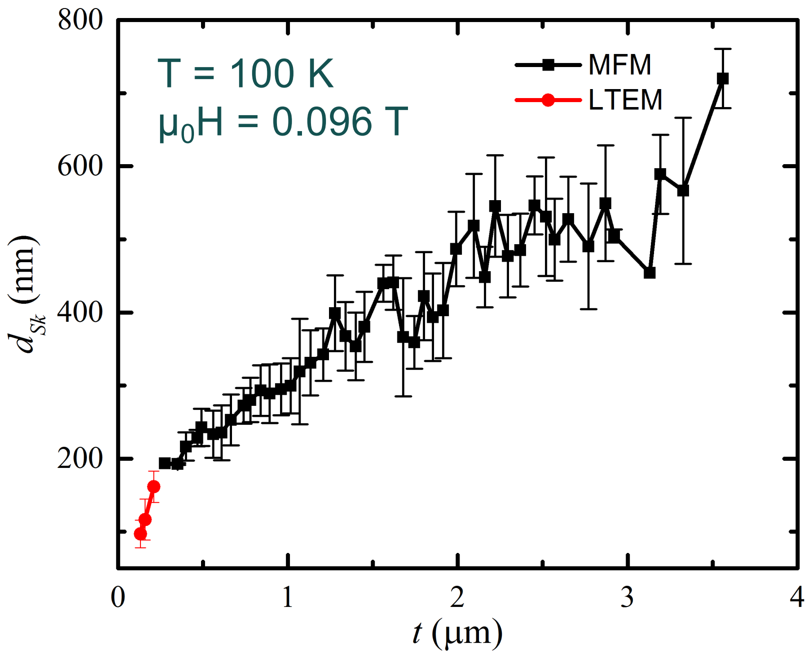

Skyrmion size vs thickness

Robustness against in-plane magnetic field

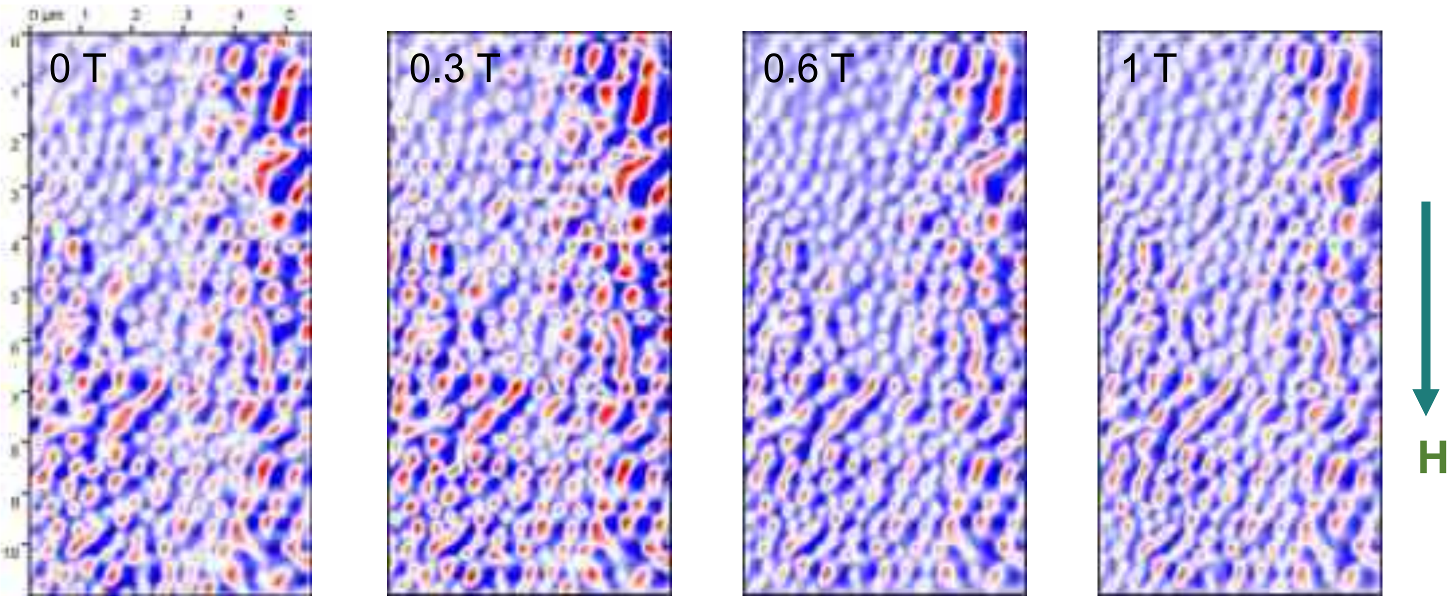

MFM images of metastable Néel skyrmions in a uniform lamella of thickness 1 µm

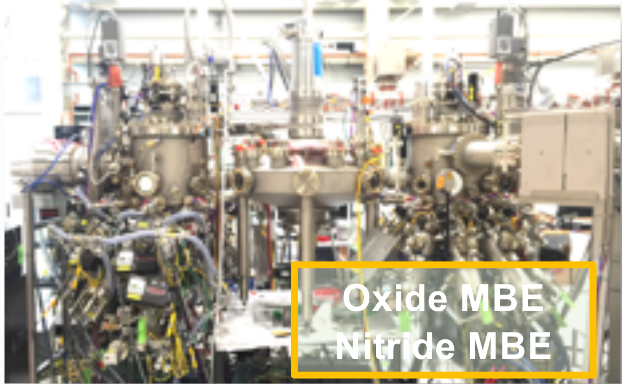

Thin film deposition

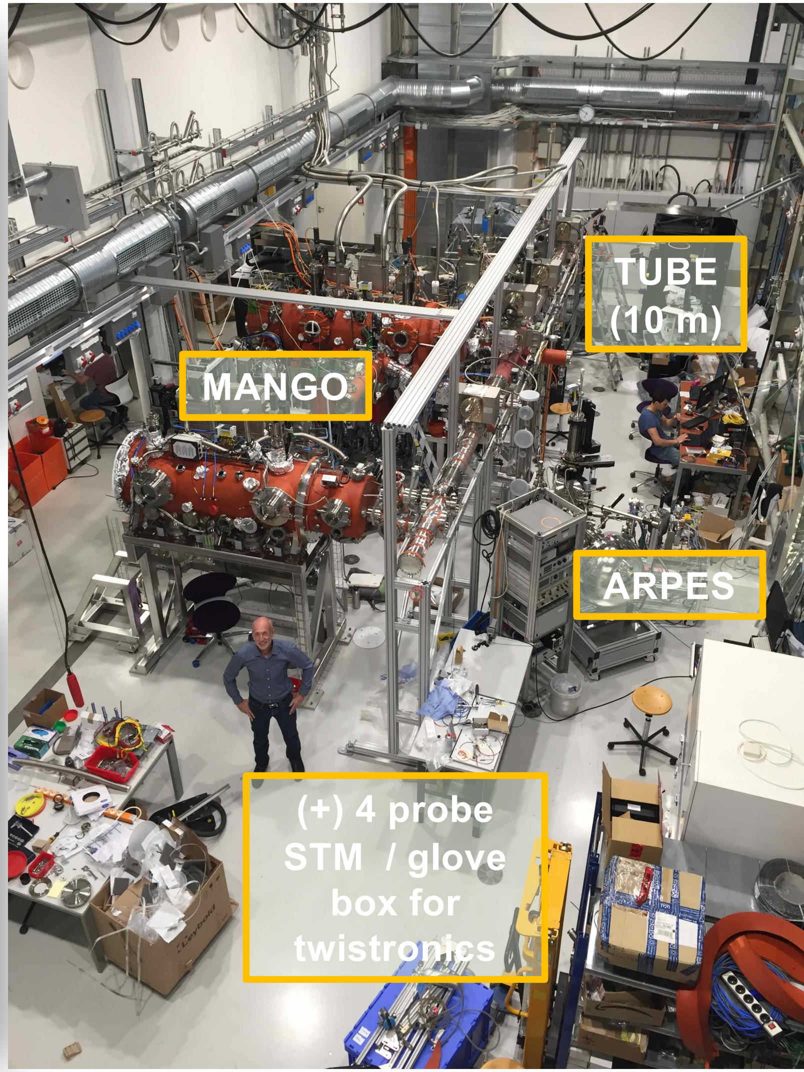

Conventional versus ionic liquid gating

Metal-**I**nsulator-**S**emiconductor (MIS) FET structure

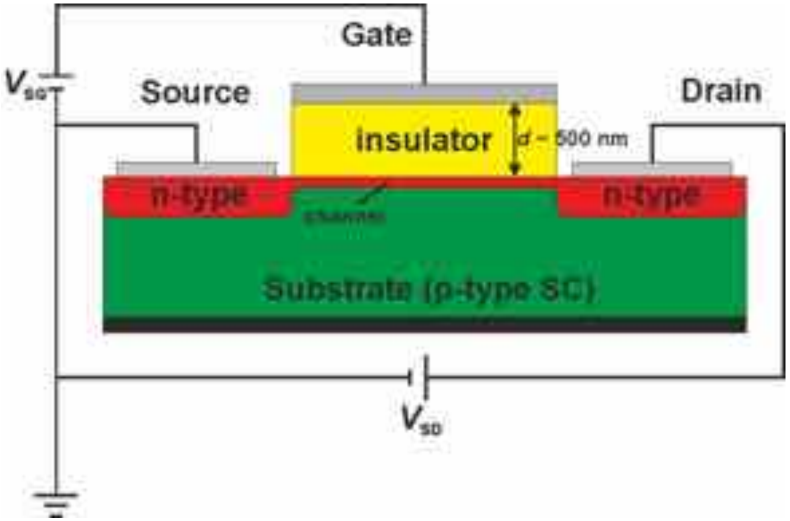

- Insulating layer ≈ 100 nm
- Capacitance ≈ 10 – 50 nF cm^{-2}
- Charge carrier density ≈ 10^{13} cm^{-2}
- High gate voltages necessary

Electrochemical **D**ouble **L**ayer (EDL) FET structure

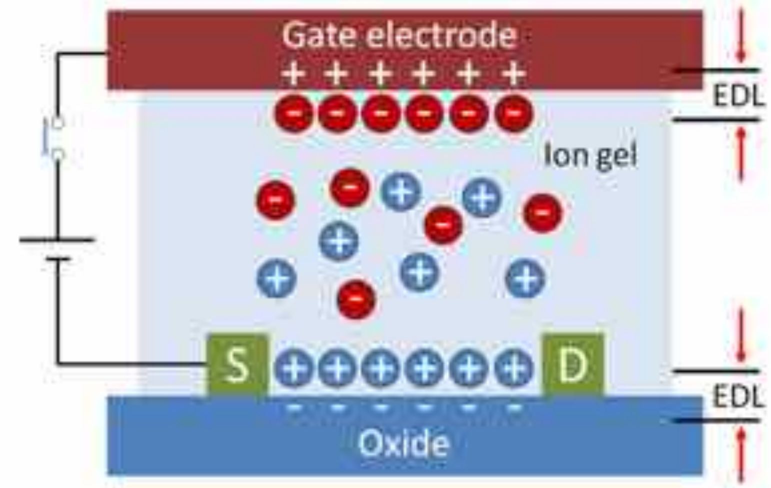

- EDL ≈ 1 nm
- Capacitance ≈ 1 μF cm^{-2}
- **Charge carrier density ≈ 10^{15} cm^{-2}**
- Gate voltage <3V

Ionic Liquid Gate induced Suppression of MIT

10 nm $VO_2/TiO_2(001)$

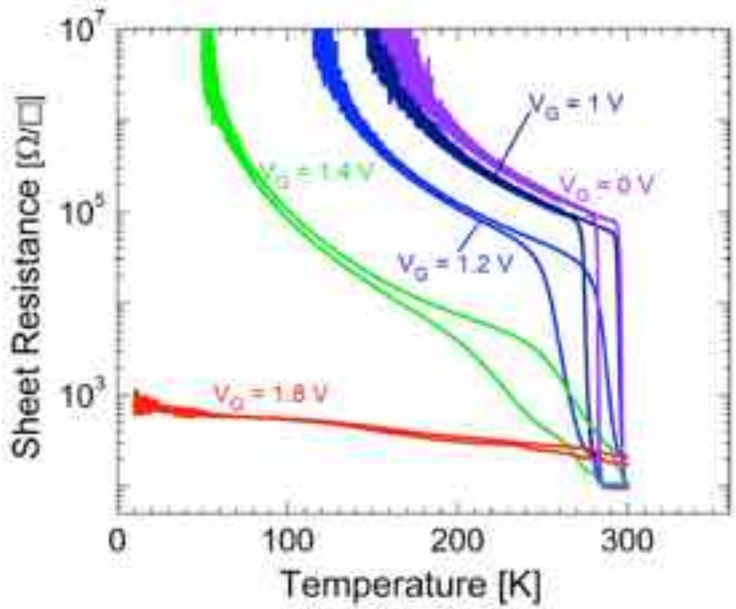

20 nm $VO_2/Al_2O_3(001)$

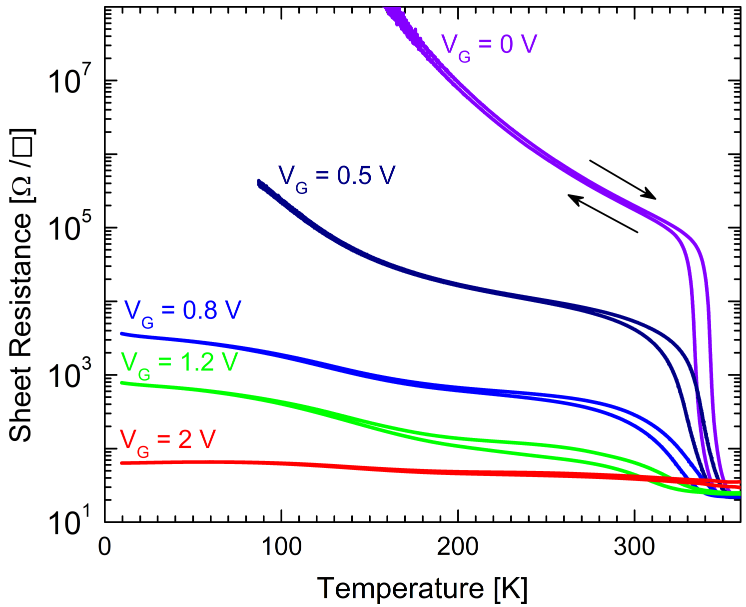

- MIT is suppressed down to 10K with the application of gate voltage.
- No signature of residual MIT
  → The entire film is metallized.

Science (2013), PNAS (2015, 2016), Nano Lett. (2013, 2016), Adv. Mater. (2016, 2017)
Phys. Rev. Lett, (2016, 2017), Nano Lett. (2017), DRC (2018), Nat. Commun. (2018)

Brownmillerite – perovskite: $SrCoO_{2.5}$ – $SrCoO_3$

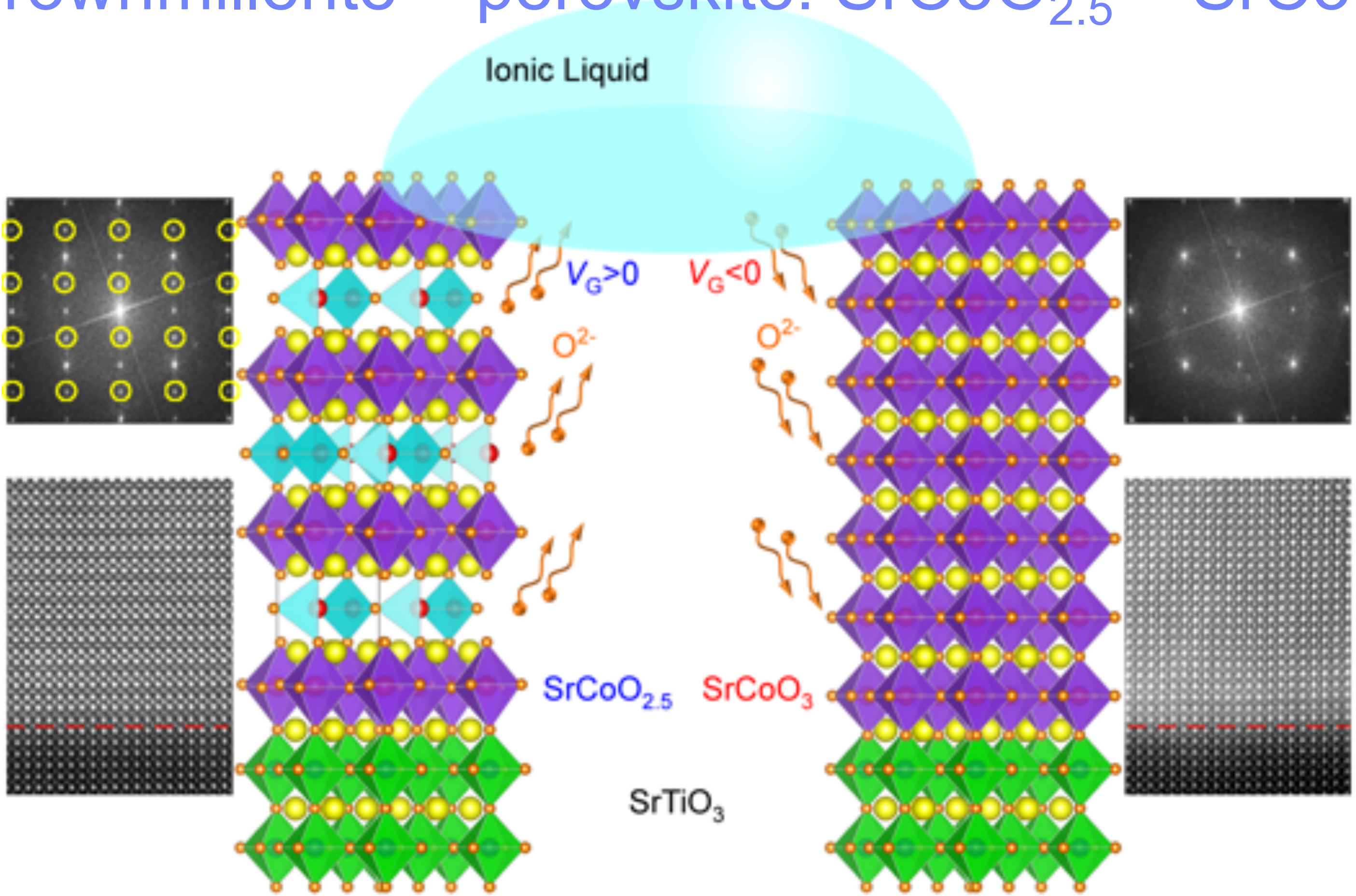

Brownmillerite
Antiferromagnet
Insulator

Perovskite
Ferromagnet
Metal

Positive and negative gate voltages applied through ionic liquid will extract oxygen from and inject oxygen into SCO, respectively, resulting in the brownmillerite $SrCoO_{2.5}$ and perovskite $SrCoO_3$.

In-situ TEM: Brownmillerite → perovskite: $SrCoO_{2.5}$ – $SrCoO_3$

V_G=-3V

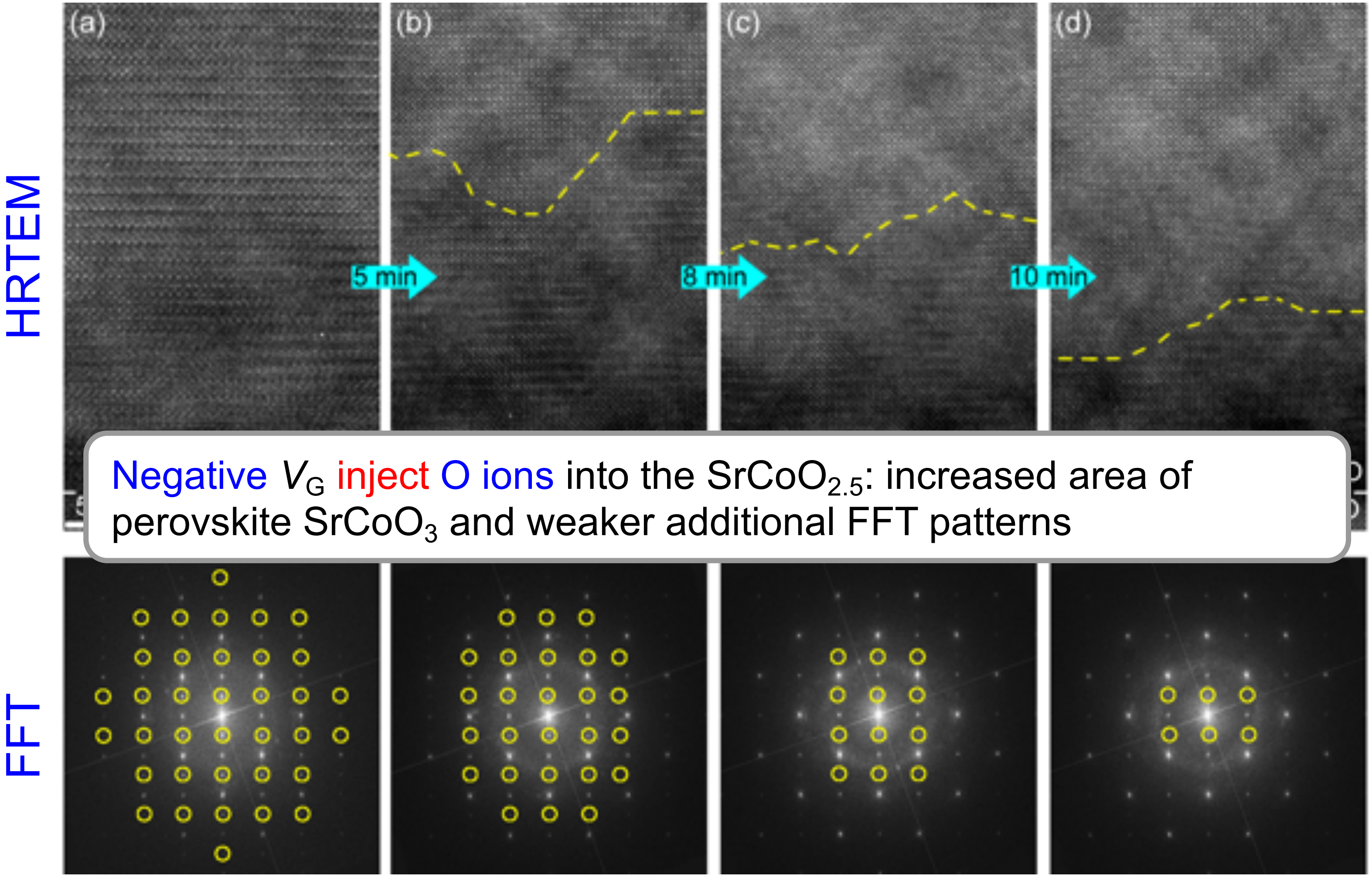

Negative V_G inject O ions into the $SrCoO_{2.5}$: increased area of perovskite $SrCoO_3$ and weaker additional FFT patterns

Time-dependent phase transition between $SrCoO_{2.5}$ and $SrCoO_3$ with ionic liquid gating. Ionic liquid on the left side.

In-situ TEM: Pervoskite → Brownmillerite : $SrCoO_3$ – $SrCoO_{2.5}$

V_G=+3V

HRTEM

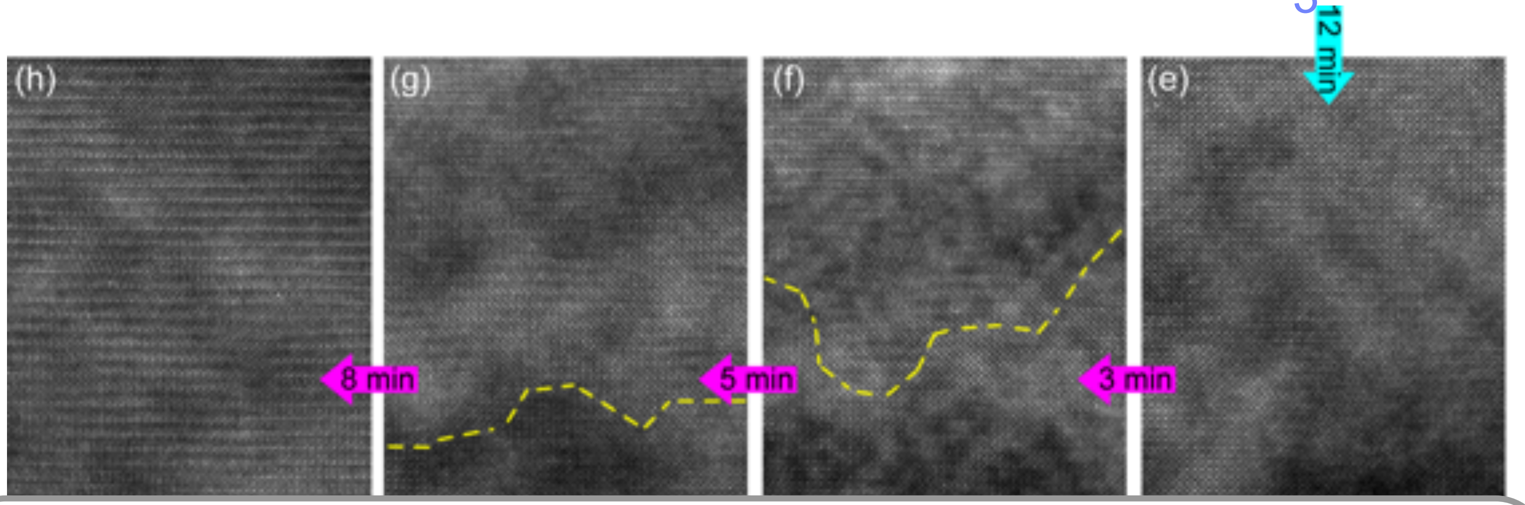

1. V_G reversibly manipulates phase transition of $SrCoO_3$-$SrCoO_{2.5}$ by injecting or extracting oxygen ions;

2. Phase transition always starts from the surface and then extends into the bulk of thin film.

FFT

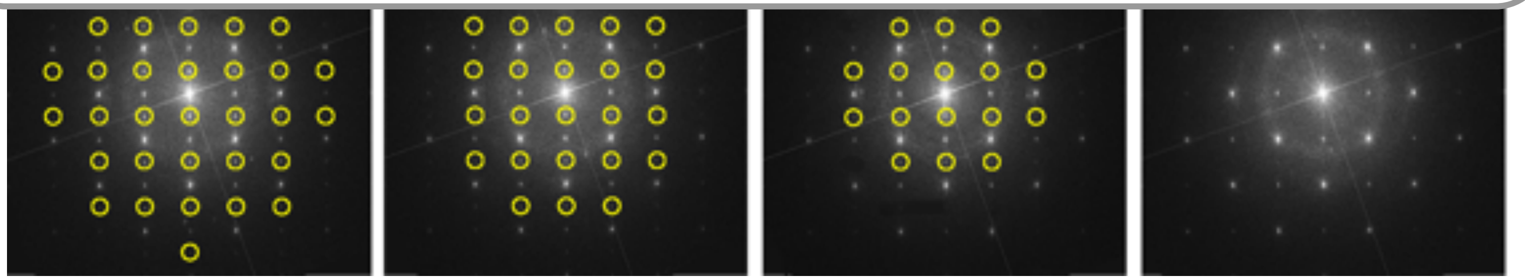

Top HRTEM, bottom FFT; yellow dashed line: rough phase boundary

IL gating controlled meso-structures

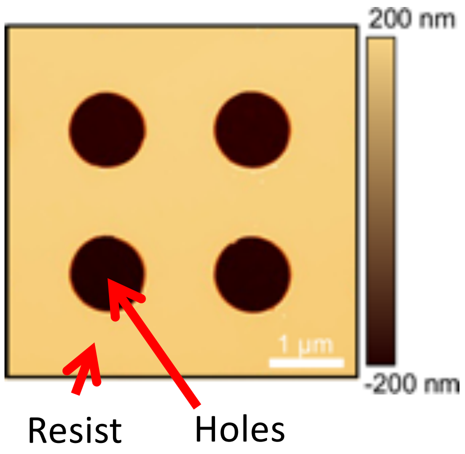

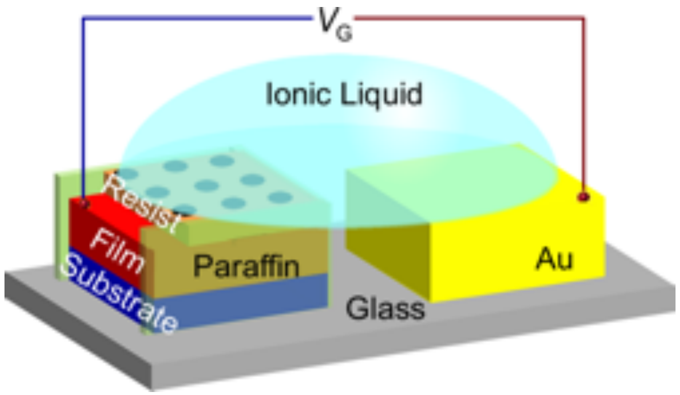

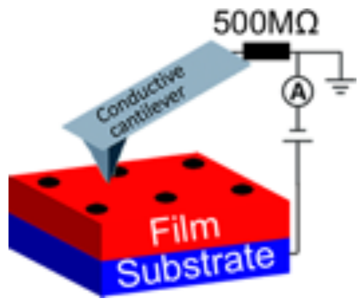

CAFM

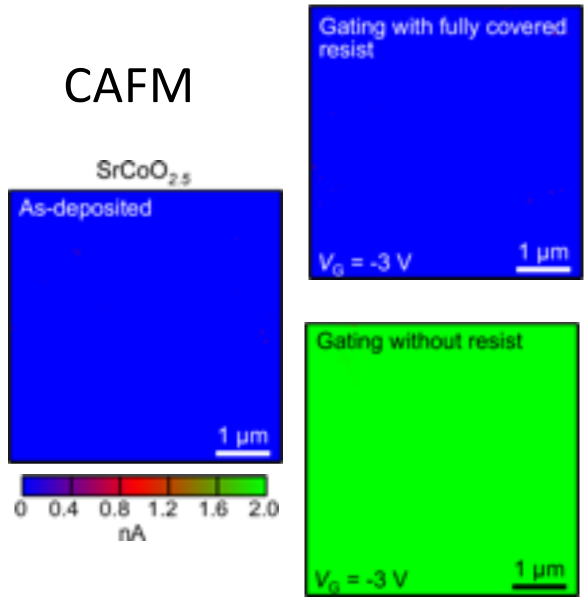

Resist can effectively obstruct the gating effect right above

IL gated patterned oxide film → 3D meso-structures

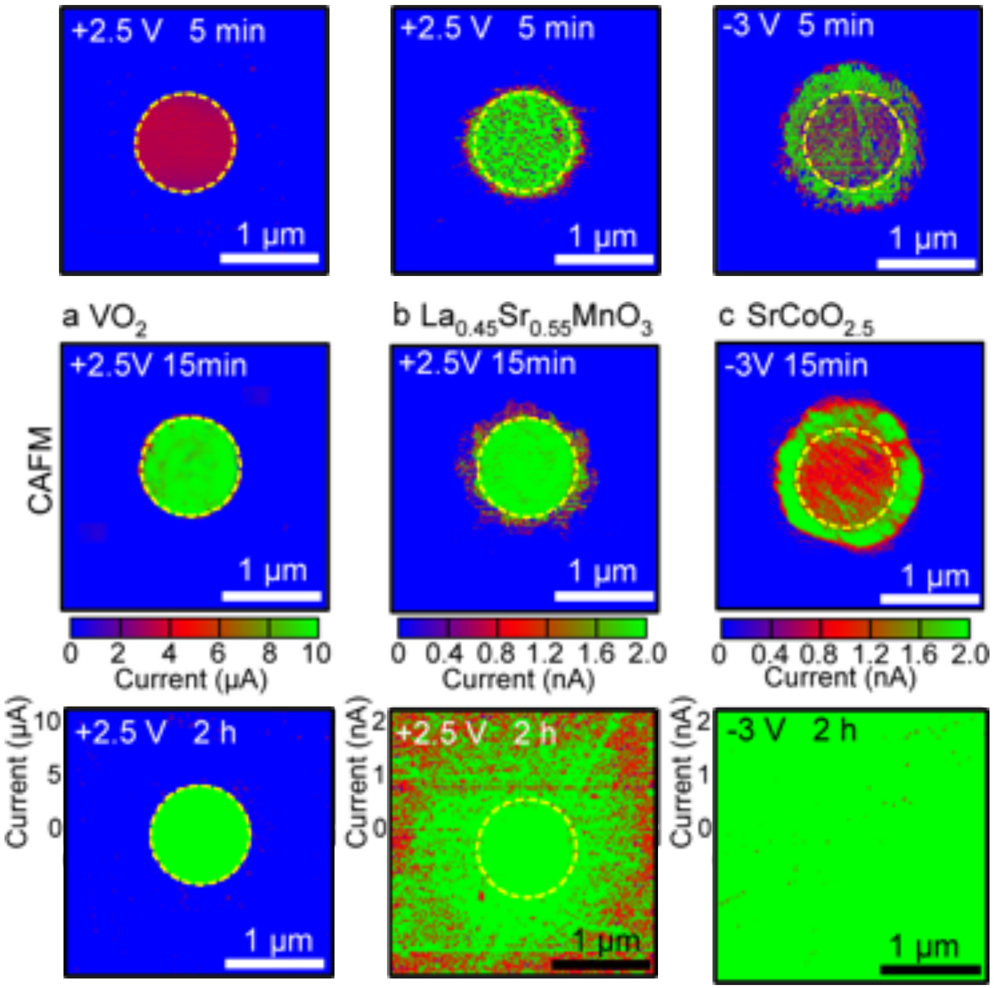

- VO_2
  Strictly limited in the resist hole: [001] O transport channel

- $La_{0.45}Sr_{0.55}MnO_3$
  Emanative pattern beyond the hole: multidirectional O transport

- $SrCoO_{2.5}$
  A more conductive ring around the hole: multidirectional O transport & perovskite/brownmilleriate interface

Multi-state phase transitions

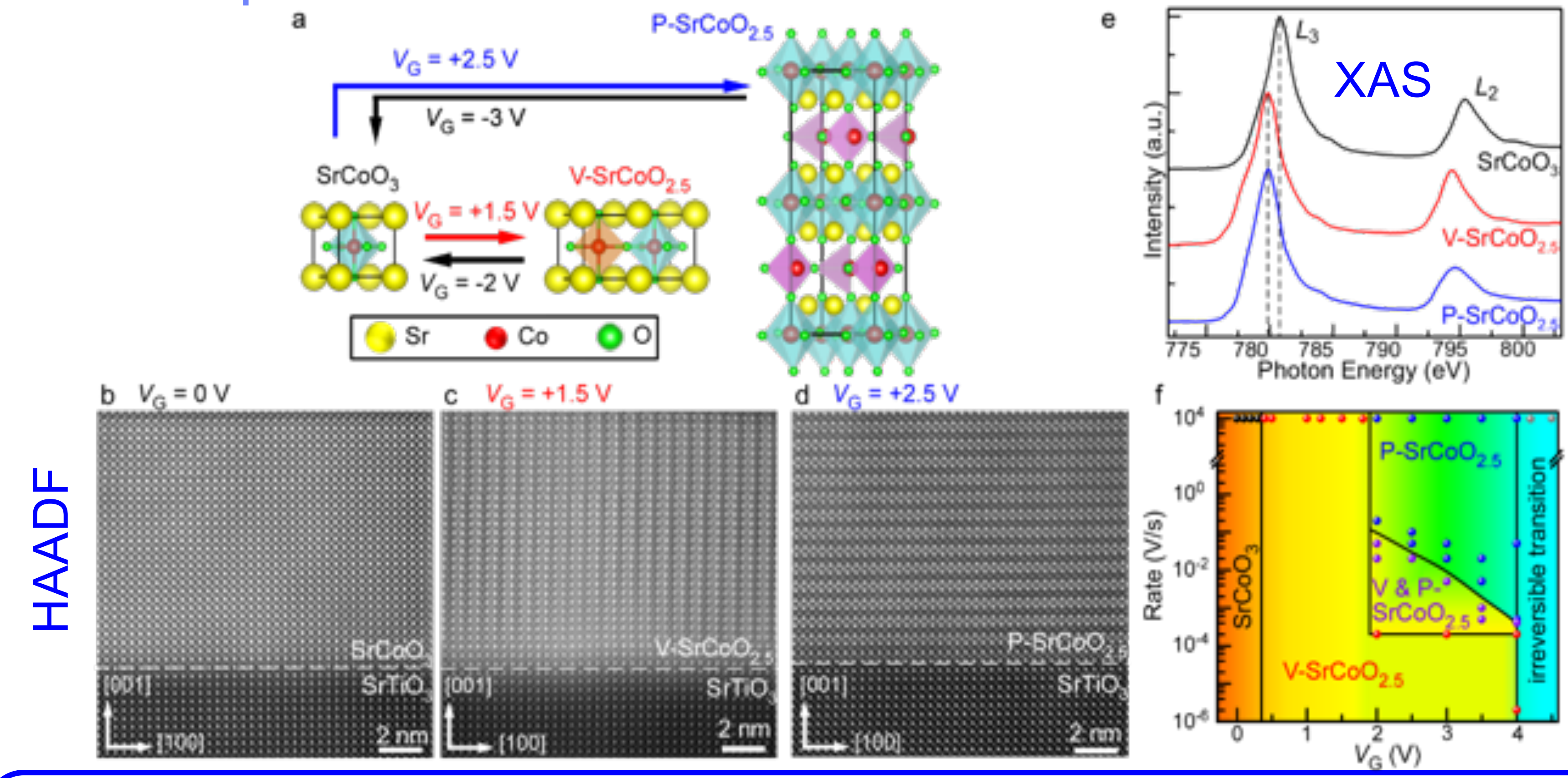

Beyond two states phase change

$SrCoO_3$ could be reversibly changed to $SrCoO_{2.5}$ with superstructure vertical and parallel to the surface using small and large gate voltages, respectively

Creation of magnetic meso-structures

P-$SrCoO_{2.5}$ & V-$SrCoO_{2.5}$

CAFM

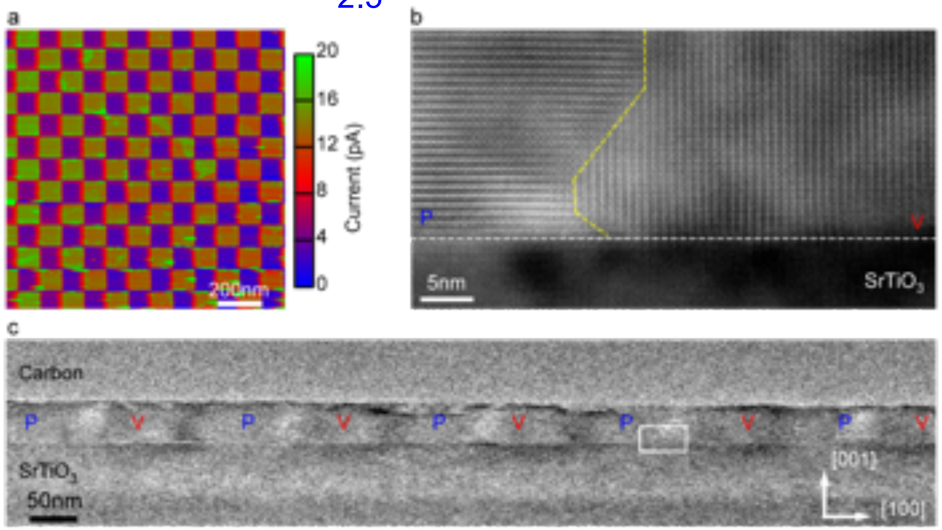

$SrCoO_3$ & V-$SrCoO_{2.5}$

CAFM

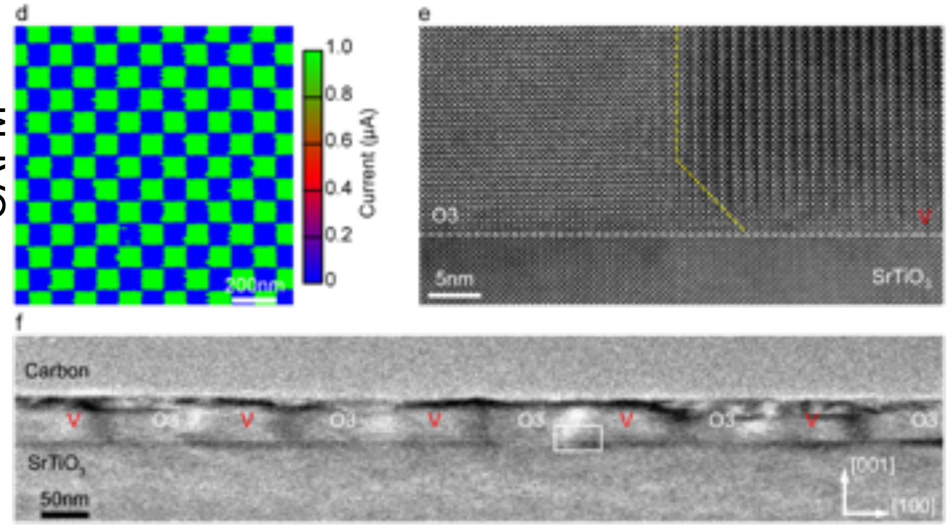

- Nanoscale gridding (~100nm) made by patterned ionic liquid gating

Chiral spintronics:
Chiral and spatial spin textures

- **Anti-skyrmions**
  - Observed in several tetragonal inverse Heuslers
  - Anti-skrymion size & helical wavelength increase with thickness
  - ”elliptical” twinned skyrmions found in same system
- **Important technological applications – Racetrack Memory**
  - DW velocities > 1,000 m/sec in synthetic antiferromagnets
  - 3T Single DW Racetrack - replacement for SRAM
  - Promises 3T device with SRAM performance but increased density, much lower energy consumption & non-volatility (fast start-up)
- **Artificial spin textures**
  - Using ionic liquid gate induced FM and AFM (2x) phases can create wide varierty of spatial spin textures – racetrack, spin liquid…

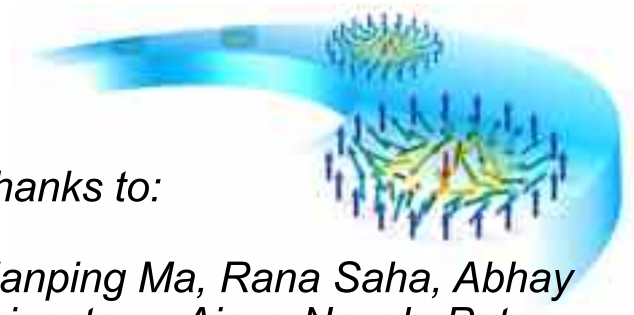

Thanks to:

Tianping Ma, Rana Saha, Abhay Srivastava, Ajaya Nayak, Peter Werner, Robin Blasing, Kai-Uwe Demasius, MPI-Halle

Vivek Kumar, Roshnee Sahoo, Parul Devi, Claudia Felser MPI-cpfs

Börge Göbel, Ingrid Mertig MLU, Halle

See-Hun Yang, Chirag Garg, IBM Research - Almaden

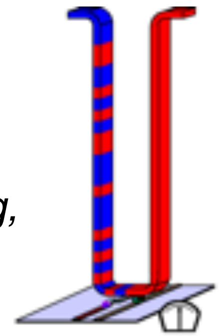

Nayak *et al.* Nature (2017)
Yang *et al.* Nat. Phys. (2019)
Sana *et al.* Nat Comm. (2019)
Srivastava *et al.* Adv. Mater. (2019)

Innately 3D memory and logic devices

Today: 2D

Future: innately 3D

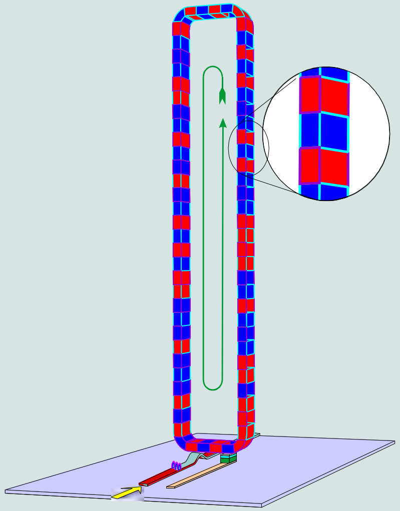

Racetrack Memory

10 to 100 times the storage capacity of conventional solid state memory

→ Could displace flash memory and hard disk drives

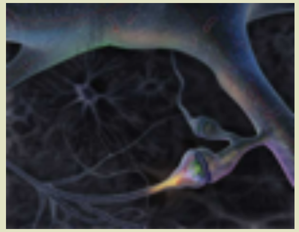

Cognitive Devices

emulating synaptic functions in a solid state device

→ *Million times more energy efficient than charge based computers*